University of Reading

A mixed-phase bulk orographic precipitation model with embedded convection

Article

Published Version

Creative Commons: Attribution 3.0 (CC-BY)

Cannon, D., Kirshbaum, D. J. and Gray, S. L. (2013) A mixed-phase bulk orographic precipitation model with embedded convection. Quarterly Journal of the Royal Meteorological Society, 140 (683). pp. 1997-2012. ISSN 1477-870X doi: https://doi.org/10.1002/qj.2269 Available at https://centaur.reading.ac.uk/35015/

It is advisable to refer to the publisher's version if you intend to cite from the work. See Guidance on citing.
Published version at: http://dx.doi.org/10.1002/qj.2269
To link to this article DOI: http://dx.doi.org/10.1002/qj.2269

Publisher: Royal Meteorological Society

All outputs in CentAUR are protected by Intellectual Property Rights law, including copyright law. Copyright and IPR is retained by the creators or other copyright holders. Terms and conditions for use of this material are defined in the End User Agreement.

www.reading.ac.uk/centaur

CentAUR

University of Reading

Central Archive at the University of Reading

Reading's research outputs online

RMetS
Royal Meteorological Society

A mixed-phase bulk orographic precipitation model with embedded convection†

Dirk J. Cannon,[a]* Daniel J. Kirshbaum[a,b] and Suzanne L. Gray[a]

[a]*Department of Meteorology, University of Reading, UK*
[b]*Department of Atmospheric and Oceanic Sciences, McGill University, Montréal, Québec, Canada*

*Correspondence to: D. J. Cannon, Department of Meteorology, University of Reading, Reading, RG6 6BB, UK.
E-mail: d.j.cannon@reading.ac.uk

A novel analytical model for mixed-phase, unblocked and unseeded orographic precipitation with embedded convection is developed and evaluated. The model takes an idealized background flow and terrain geometry and calculates the area-averaged precipitation rate and other microphysical quantities. The results provide insight into key physical processes, including cloud condensation, vapour deposition, evaporation and sublimation, as well as precipitation formation and sedimentation (fallout). To account for embedded convection in nominally stratiform clouds, diagnostics for purely convective and purely stratiform clouds are calculated independently and combined using weighting functions based on relevant dynamical and microphysical time-scales. An in-depth description of the model is presented, as well as a quantitative assessment of its performance against idealized, convection-permitting numerical simulations with a sophisticated microphysics parametrization. The model is found to reproduce the simulation diagnostics accurately over most of the parameter space considered.

Key Words: precipitation efficiency; condensation; drying ratio; mixed-phase microphysics

Received 15 May 2013; Revised 8 August 2013; Accepted 3 October 2013; Published online in Wiley Online Library

1. Introduction

Orographic precipitation involves complex interactions between nonlinear dynamical and microphysical processes and hence a full conceptual understanding remains elusive. To improve this understanding and aid the development of numerical weather prediction models, numerous field campaigns have recently been conducted (Bougeault *et al.*, 2001; Stoelinga *et al.*, 2003; Damiani *et al.*, 2008; Wulfmeyer *et al.*, 2008). These studies have documented precipitation events over different regions, assessed the accuracy with which high-resolution numerical simulations reproduce these events and enabled intensive case study analyses. In addition, numerous real-case (Rotunno and Ferretti, 2001) and idealized (Kirshbaum and Smith, 2008) numerical modelling studies have highlighted the basic environmental and terrain-related controls on orographic precipitation amounts and distributions.

Despite these advancements, a generalized quantitative understanding of orographic precipitation has yet to be achieved. Ideally, such an understanding should be conveyed by analytical models that capture the dominant processes yet allow for simplified physical interpretations. Various models of mechanically forced orographic precipitation have been developed over the past few decades. These include simple upslope or parcel models (Sawyer, 1956), models of the seeder-feeder mechanism (Bader and Roach, 1977; Choularton and Perry, 1986) and models utilizing linear hydrostatic mountain-wave dynamics (Smith and Barstad, 2004; Kunz and Kottmeier, 2006; Barstad and Schüller, 2011), which can predict orographic precipitation distributions for given upstream conditions and terrain geometry. Although these models have shown promise in some situations, their applicability is often restricted to specific types of flow. In particular, few models have considered the important impacts of mixed-phase microphysics (exceptions include Kunz and Kottmeier, 2006; Barstad and Schüller, 2011) and none have considered the impact of embedded moist convection, which commonly develops in orographic clouds and can be critically important for precipitation enhancement (Kirshbaum and Durran, 2004; Fuhrer and Schär, 2005; Cannon *et al.*, 2012). This is not surprising, given the strong nonlinearity of convective processes and their complex interactions with the parent orographic cloud.

In this study we develop an analytical model that predicts the area-averaged precipitation in a mixed-phase orographic cloud with embedded convection. Due to the complexity of these processes, the model is greatly simplified to maintain analytical tractability. Our principal objectives with this model are (i) to take a first step toward the simultaneous consideration of two key

†The copyright line for this article was changed on 18 February 2014 after original online publication.

© 2013 The Authors. *Quarterly Journal of the Royal Meteorological Society* published by John Wiley & Sons Ltd on behalf of the Royal Meteorological Society.
This is an open access article under the terms of the Creative Commons Attribution License, which permits use, distribution and reproduction in any medium, provided the original work is properly cited.

processes (embedded convection and detailed microphysics) and (ii) to provide a framework for understanding the interactions between convection and microphysics in orographic clouds. Predictions from this model are compared against nonlinear numerical simulations, showing good agreement over a wide range of parameter space. Section 2 describes the numerical simulations and the important diagnostic quantities that are used to interpret them. The formulation of the analytical model is described in section 3 and its strengths and deficiencies are interpreted relative to the numerical simulations. Conclusions are presented in section 4. To aid the reader, a list of commonly used abbreviations and symbols is provided in Appendix B.

2. Numerical model

2.1. Simulation set-up

The analytical model developed in this study is evaluated against the idealized simulation results of Cannon *et al.* (2012). As a more detailed description of the simulation set-up and results was provided in that article, only a brief summary is given here. These simulations used the Weather Research and Forecasting (WRF) model version 3.1, which is non-hydrostatic and fully compressible (Skamarock *et al.*, 2008). A set of 'convection-permitting' (CP) simulations were performed using a three-dimensional domain of length $L_x = 1800$ km (the cross-ridge direction), width $L_y = 30$ km (the ridge-parallel direction) and height $L_z = 15$ km (the vertical direction). These simulations were conducted using a horizontal grid length of $\Delta x = 1$ km and with uniformly distributed random upstream moisture perturbations (of maximum amplitude 5%) to initiate convection. Subgrid-scale turbulent kinetic energy (TKE) was parametrized using a 1.5-order TKE closure, whilst cloud and precipitation microphysics was parametrized using the mixed-phase Thompson scheme (Thompson *et al.*, 2004, 2008). Sensitivity tests were also conducted with the Morrison microphysics parametrization (Morrison and Pinto, 2005; Morrison *et al.*, 2005; Morrison and Thompson, 2009). Whilst these tests showed different hydrometeor compositions and quantitative precipitation amounts, the sensitivity of the results to moist stability and mountain geometry remained intact. This is also consistent with Kirshbaum and Smith (2008), who performed similar simulations with an older version of the Thompson scheme and the WRF single-moment 6-class (WSM6) parametrization (Hong *et al.*, 2004). For simplicity, no surface-layer scheme or boundary-layer parametrization was employed, however surface drag was imposed using a bulk aerodynamic drag coefficient, $C_d = 0.01$. The Coriolis force was applied to perturbations from the geostrophically balanced basic state with the Coriolis parameter $f = 10^{-4}\ \mathrm{s}^{-1}$.

To quantify the impact of embedded convection on orographic precipitation, an additional suite of 'laminar' (LAM) simulations was conducted in which convection was artificially suppressed, allowing the air to ascend the mountain smoothly. To suppress convection, the LAM simulations were run in two dimensions (2D) at coarser resolution, with no upstream moisture perturbations and with artificial sixth-order diffusion to help suppress the growth of unstable perturbations. As can be seen from the cross-sections of potential temperature and hydrometeor mixing ratios in Figure 1, whereas moist convection freely developed in the CP simulations, it was successfully suppressed in the LAM simulations without substantially modifying the mountain-scale flow dynamics.

The simulation set-up is shown schematically in Figure 2, which depicts a moist flow incident on a one-dimensional (1D) Gaussian ridge of half-width a_m and maximum height h_m, centred at $x = x_m$. A range of a_m and h_m values is considered: $a_m = 15$, 30 and 60 km and $h_m = 1$ and 2 km. Whilst clearly an idealization, this range of mountain dimensions encompasses a broad range

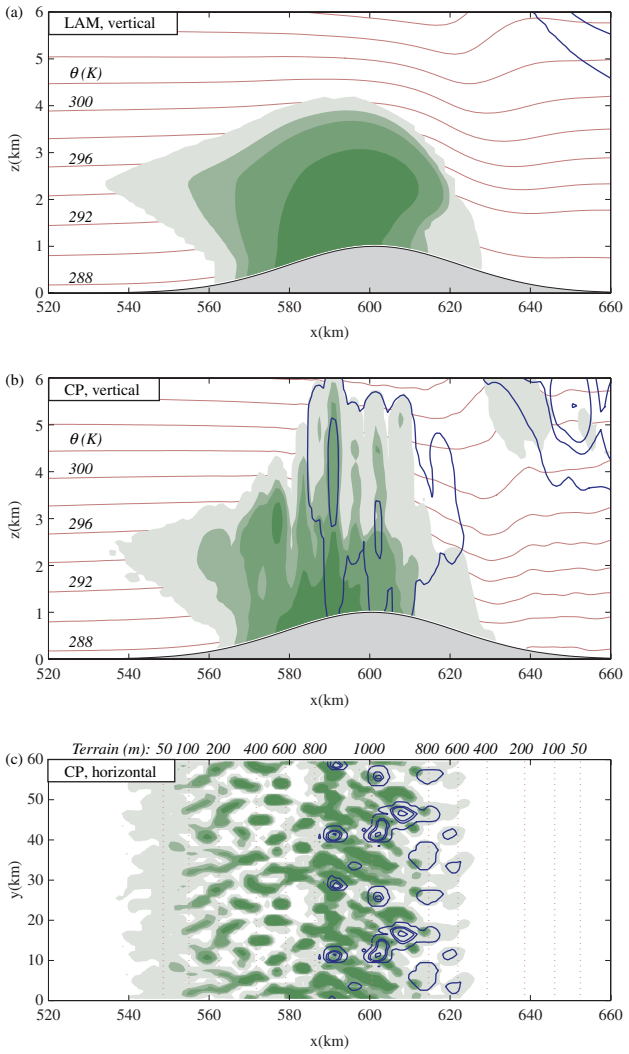

Figure 1. Cross-sections of the liquid water (cloud and rain) mixing ratio, q_l (grey filled contours, green online), and frozen water (ice, snow and graupel) mixing ratio, q_f (black contours, dark blue online), at $t = 12$ h. Panel (a) shows the LAM simulation and panels (b) and (c) the CP simulation for which $a_m = 30$ km, $h_m = 1$ km and $T_s = 287.5$ K. For the vertical cross-sections (a, b), background contours of y-averaged potential temperature (red online) are shown for every 2 K in unsaturated regions. In (c), a horizontal cross-section of the same CP simulation is shown (at $z = 2$ km). Terrain contours are depicted as dotted lines (red online) and the plot from $y = 0 \rightarrow 30$ km is repeated from $y = 30 \rightarrow 60$ km for ease of viewing. For all panels, the mixing ratio contours correspond to $[0.001, 0.1, 0.2, 0.5]$ g kg^{-1}. No horizontal cross-section is shown for the LAM simulation, as they are two-dimensional. This figure is available in colour online at wileyonlinelibrary.com/journal/qj

of mid-latitude mountains. For example, the highest and widest ridges resemble the North American Cascades and southern Andes chains, whereas the shorter, narrower mountains resemble the UK Pennines and the Oregon Coastal Range.

The hydrostatically balanced and horizontally uniform initial flows are based on a six-year precipitation-weighted climatology of the mid-latitude mountain ranges along the west coasts of the Americas (Kirshbaum and Smith, 2008). For simplicity, these flows are defined by a few basic parameters: a uniform background cross-barrier wind speed $U = 15\ \mathrm{m\,s}^{-1}$, a surface temperature T_s, a dry Brunt-Väisälä frequency $N_d = 0.01\ \mathrm{s}^{-1}$ and a relative humidity $RH = 90\%$ in the troposphere (up to 10 km); $N_d = 0.02\ \mathrm{s}^{-1}$ and $RH = 30\%$ in the stratosphere (above 10 km). The saturation vapour pressure with respect to liquid (ice) was used to calculate the water-vapour mixing ratios below (above) the freezing level. In these flows, the dry Froude number ($Fr = U/N_d h_m$) is at least 0.75 and, as clouds act to increase the effective Fr, upstream flow blocking has a generally modest influence on the flow dynamics.

© 2013 The Authors. *Quarterly Journal of the Royal Meteorological Society* published by John Wiley & Sons Ltd on behalf of the Royal Meteorological Society.

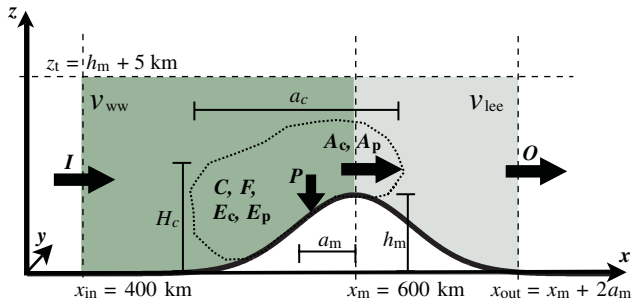

Figure 2. A schematic showing the fluxes and conversion rates of water substance in the simulations of Cannon *et al.* (2012). Symbols are as defined in the text. This figure is available in colour online at wileyonlinelibrary.com/journal/qj

To examine the flow response to changing moist stability and microphysical composition, a range of T_s values between 277.5 and 287.5 K, in intervals of 2.5 K, was considered. The warmer temperatures are associated with both increasing potential instability (not shown) and conditional instability, which is apparent from the Convective Available Potential Energy (CAPE) of surface-based parcels listed in Table 1. Other relevant metrics in Table 1 include the Convective Inhibition (CIN) and the heights of the lifting condensation level (z_{LCL}), level of free convection (z_{LFC}) and level of neutral buoyancy (z_{LNB}). The height of the environmental freezing level is given by z_f.

2.2. Diagnostics

The total control volume in Figure 2 ($\mathcal{V}$) is made up of the windward and lee volumes ($\mathcal{V}_{ww}$ and $\mathcal{V}_{lee}$ respectively) and is bounded by surfaces defined by $x = x_{in}$, $x = x_{out}$, $z = h(x)$ (where h is the mountain elevation) and $z = z_t$. This volume contains the orographic cap cloud (dotted) which has characteristic width $a_c < x_{out} - x_{in}$ and depth $H_c < z_t$. Thick arrows depict the vertically integrated horizontal water vapour flux (or 'influx', I) through the surface $x = x_{in}$ and the surface precipitation rate (P) through $z = h(x)$ (between x_{in} and x_{out}). Also shown are the rate of advection of cloud and precipitation to the lee through the vertical surface $x = x_m$ (A_c and A_p respectively) and the downstream vertically integrated horizontal water flux (or 'outflux', O) through the vertical surface $x = x_{out}$. The phase changes of water within the cloud are described by the condensation rate (C) (which as defined here includes both vapour condensation to liquid cloud and deposition to ice), the precipitation formation rate (F) and the upslope evaporation rates of cloud (E_c) and precipitation (E_p). Note that whilst C and F are evaluated over the entire control volume ($\mathcal{V}$), E_c and E_p are, by definition, evaluated within $\mathcal{V}_{ww}$. All fluxes and conversion rates are averaged in y and from 12–18 h to obtain robust statistics from the quasi-2D, quasi-steady mountain airflow. All of these dimensional diagnostics have units of kg m^{-1} s^{-1}.

The diagnostic trends can be more succinctly visualized through the following non-dimensional diagnostics (Smith *et al.*, 2003; Barstad *et al.*, 2007; Kirshbaum and Smith, 2008). The condensation ratio, $CR = C/I$, represents the proportion of incident moisture that condenses within $\mathcal{V}$. The upslope cloud evaporation efficiency, $EE_c = E_c/C$, is the proportion of this condensate (within $\mathcal{V}$) that evaporates within $\mathcal{V}_{ww}$. The formation efficiency, $FE = F/C$, is the proportion of condensate that forms precipitation (within $\mathcal{V}$) and the sedimentation efficiency, $SE = P/F$, is the proportion of precipitation that, once formed, reaches the surface between x_{in} and x_{out}. The precipitation efficiency, $PE = FE \times SE = P/C$ therefore represents the proportion of condensate that forms precipitation *and* reaches the surface between x_{in} and x_{out}. Finally, the drying ratio, $DR = CR \times PE = P/I$ represents the proportion of incident moisture that is converted to surface precipitation between x_{in} and x_{out}.

3. The analytical model

In this section, the analytical model is described and compared quantitatively with the simulation results of Cannon *et al.* (2012). This model is applicable to orographic flows that are quasi-two-dimensional, unblocked, unseeded by larger-scale precipitation and initially unsaturated (as in the simulations described in section 2). Firstly, analytical equivalents for the diagnostics defined in section 2.2 will be derived. To differentiate them from simulation diagnostics, which are written in standard font, these are written in 'blackboard bold' font (e.g. $\mathbb{A}$, $\mathbb{B}$, $\mathbb{C}$). For ease of reference, each result is given a unique name defined by a_m, h_m, type (e.g. LAM or CP) and an integer value of T_s. For example, the a30-h1-LAM-T277 result corresponds to the case with $a_m = 30$ km, $h_m = 1$ km, and is purely mechanically forced (laminar) with $T_s = 277.5$ K.

In reality (and in the CP simulations) the flow dynamics are neither purely mechanically forced or convective but rather fall in between these two extremes. To determine the relative contributions of mechanically forced and convective processes, simple weighting functions are used (based on the schematic in Figure 3). In order to be lifted via convective processes, water vapour (which enters the cloud region at rate $\mathbb{I}$) must first cross its LFC, then undergo convective ascent. The respective moisture fluxes associated with these processes are $\mathbb{R}_{LFC}$ and $\mathbb{R}_{CONV}$ respectively. Air that is either not raised to its LFC, or is raised to its LFC but lacks the residence time in the cloud to undergo convective overturning before reaching the lee, experiences only mechanically forced ascent. The respective moisture fluxes associated with these processes are $\mathbb{R}_{LAM1}$ and $\mathbb{R}_{LAM2}$, respectively. Given this framework, steady-state equations governing the conservation of water substance within the cloud region can be written as

$$\mathbb{I} = \mathbb{R}_{LFC} + \mathbb{R}_{LAM1}, \quad (1)$$

$$\mathbb{R}_{LFC} = \mathbb{R}_{CONV} + \mathbb{R}_{LAM2}, \quad (2)$$

$$\mathbb{R}_{LAM} = \mathbb{R}_{LAM1} + \mathbb{R}_{LAM2}, \quad (3)$$

where the total proportion of $\mathbb{I}$ that is lifted purely mechanically ($\mathbb{R}_{LAM}$) is equal to the sum of the contributions from both pathways that include only mechanical lifting. For simplicity, the moisture fluxes ($\mathbb{R}$) are treated as linear functions of the mass (per unit length) of moisture in the initial state (M) and so $\mathbb{R} = M/\tau$,

Table 1. Characteristics of the initial atmospheric profiles (from Cannon *et al.*, 2012). All parcel displacement metrics assume the parcel originates at the surface ($z_i = 0$ in the notation of section 3). Symbols are defined in the text.

Sounding	T_s (K)	*CAPE* (J kg^{-1})	*CIN* (J kg^{-1})	z_{LCL} (km)	z_{LFC} (km)	z_{LNB} (km)	z_f (km)
*T*277	277.5	0.0	–	0.19	–	–	0.65
*T*280	280.0	7.2	10.4	0.19	1.17	2.89	1.03
*T*282	282.5	73.8	7.8	0.19	0.83	4.58	1.42
*T*285	285.0	218.9	7.1	0.20	0.71	6.12	1.81
*T*287	287.5	481.2	6.7	0.21	0.65	7.74	2.21

© 2013 The Authors. *Quarterly Journal of the Royal Meteorological Society* published by John Wiley & Sons Ltd on behalf of the Royal Meteorological Society.

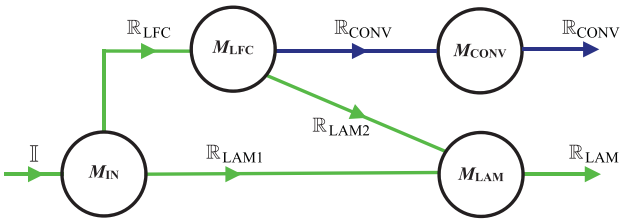

Figure 3. The weighting between the purely mechanically forced (laminar) and convective flow regimes. Moisture enters the cloud region at rate $\mathbb{I}$ and is forcibly lifted over the mountain at rate $\mathbb{R}_{LAM1}$ and to its level of free convection (LFC) at a rate $\mathbb{R}_{LFC}$. Moisture lifted past its LFC is then lifted further via convective overturning at a rate $\mathbb{R}_{CONV}$ and is swept up and over to the lee at a rate $\mathbb{R}_{LAM2}$. Grey lines (green online) indicate purely mechanically forced pathways and black lines (blue online) indicate pathways involving convective lifting. The M terms denote the mass of water within the cloud region at each stage of the lifting process. This figure is available in colour online at wileyonlinelibrary.com/journal/qj

where τ is the time-scale for the transition of moisture between the initial and new state (and is independent of M). The time-scale associated with moisture that is lifted mechanically and remains below its LFC (i.e. that associated with $\mathbb{R}_{LAM1}$) is estimated as

$$\tau_{LAM1} = \frac{h_m}{w_{LAM}} = \frac{h_m}{U\,(h_m/a_c)}, \tag{4}$$

and so is equal to the advective time-scale, $\tau_a = a_c/U$, where $w_{LAM} = Uh_m/a_c$ is a typical vertical velocity of the parcel in a mechanically lifted flow. The cloud width, a_c, is estimated as the absolute difference between the horizontal position at which the surface crosses the LCL of a surface parcel and that of the mountain peak. The time-scale associated with the mechanically forced lifting of moisture from its initial position to its LFC (i.e. that associated with $\mathbb{R}_{LFC}$) is estimated as

$$\tau_{LFC} = \frac{z_{LFC}}{w_{LAM}} = \tau_a \frac{z_{LFC}}{h_m}, \tag{5}$$

where z_{LFC} is assumed to be characteristic of the amount of lifting required for air parcels to reach their LFC (as in Table 1). The time-scale for convective overturning (i.e. that associated with $\mathbb{R}_{CONV}$) is defined as

$$\tau_{CONV} = \frac{z_{LNB} - z_{LFC}}{w_{CONV}} = \frac{z_{LNB} - z_{LFC}}{\gamma\sqrt{CAPE}}, \tag{6}$$

where (as for z_{LFC}) z_{LNB} and CAPE are calculated using the (dry/moist adiabatic) ascent of a surface parcel (as in Table 1). As this value of CAPE assumes adiabatic ascent, a dimensionless constant (γ) is included to scale the updraught velocity to one more in line with the simulations. A value of $\gamma < 1$ reflects the fact that energy is lost through the displacement of air above the parcel as it rises, as well as through entrainment, detrainment and in powering the concurrent downdraughts in the unsaturated, stably stratified air surrounding the cloud. Here we follow Renno and Ingersoll (1996) who, by treating convection as a Carnot cycle, suggested $\gamma = 0.25$. This corresponds to $w_{CONV} \approx 6\,\mathrm{m\,s^{-1}}$ when $T_s = 287.5\,\mathrm{K}$, which corresponds well to the simulated vertical velocities. There was only weak sensitivity to γ within the range $0.1 \leq \gamma \leq 0.4$ (not shown). The time-scale associated with air that is lifted to its LFC but does not undergo convective overturning (i.e. that corresponding to $\mathbb{R}_{LAM2}$) is

$$\tau_{LAM2} = \max\left[\tau_{LAM1} - \tau_{LFC},\, 0\right]. \tag{7}$$

This represents the time taken for a surface parcel to be advected via purely mechanical lifting to the lee after crossing the LFC. Unphysical negative time-scales are not permitted.

By substituting M_{IN}/τ_{LFC} for $\mathbb{R}_{LFC}$, M_{IN}/τ_{LAM1} for $\mathbb{R}_{LAM1}$, M_{LFC}/τ_{CONV} for $\mathbb{R}_{CONV}$ and M_{LFC}/τ_{LAM2} for $\mathbb{R}_{LAM2}$ in Eqs (1) and (2), it follows that

$$\mathbb{I} = M_{IN}\left(\frac{1}{\tau_{LFC}} + \frac{1}{\tau_{LAM1}}\right), \tag{8}$$

$$\mathbb{R}_{CONV} = \frac{M_{LFC}}{\tau_{CONV}} = \frac{M_{IN}}{\tau_{LFC}\left(1 + \frac{\tau_{CONV}}{\tau_{LAM2}}\right)} \tag{9}$$

and thus the respective proportions of $\mathbb{I}$ that are subject to convective and mechanically forced processes in the analytical model can be estimated as

$$\begin{aligned}\alpha_{CONV} &= \frac{\mathbb{R}_{CONV}}{\mathbb{I}} \\ &= \left(1 + \frac{\tau_{LFC}}{\tau_{LAM1}}\right)^{-1}\left(1 + \frac{\tau_{CONV}}{\tau_{LAM2}}\right)^{-1},\end{aligned} \tag{10}$$

$$\alpha_{LAM} = \frac{\mathbb{R}_{LAM}}{\mathbb{I}} = 1 - \alpha_{CONV}. \tag{11}$$

From Eqs (10) and (11) we see that when $\tau_{LFC} \gg \tau_{LAM1}$ (convection is not triggered) or when $\tau_{CONV} \gg \tau_{LAM2}$ (convective cells cannot overturn in the time available), the analytical model predicts a stratiform cloud with no embedded convection, which agrees well with the simulations of Cannon *et al.* (2012).

The remainder of this section is structured as follows. Expressions for $\mathbb{CR}$ and $\mathbb{PE}$ for a purely mechanically lifted flow are presented in sections 3.1 and 3.2 respectively, the product of which is $\mathbb{DR}$. In section 3.3, these results are quantitatively compared with the LAM simulations of Cannon *et al.* (2012) (summarized in section 2.1). Following this, $\mathbb{CR}$ and $\mathbb{PE}$ (and therefore $\mathbb{DR}$) of a purely convective flow are derived in sections 3.4 and 3.5. By combining these results with Eqs (10) and (11), diagnostics for a convection-permitting flow are derived. In section 3.6, these diagnostics are compared with those of the CP simulations, whilst in section 3.7 the analytically predicted convective enhancement in condensation and precipitation is compared with that from the simulations.

3.1. *Condensation ratio for purely mechanically lifted flow*

The analytical model takes the same atmospheric soundings and terrain profiles as those used in the simulations. To calculate $\mathbb{CR}$ for a purely mechanically lifted flow, each upstream sounding is discretized into 150 levels, equally spaced in pressure from the surface ($z = 0\,\mathrm{km}$) to the domain top ($z = 15\,\mathrm{km}$) so that all parcels possess equal hydrostatic mass. Parcels at each level are then lifted adiabatically from their initial height, $z_i(z)$, to a final height, $z_{lift,\,LAM}(z_i)$. The procedure for determining $z_{lift,\,LAM}(z_i)$ is a compromise between basic 'upslope' models that assume the air flows parallel to the terrain at all levels (Sawyer, 1956; Smith, 1979) and more complex multi-dimensional solutions to the linearized Boussinesq system (Sarker, 1967; Smith and Barstad, 2004). The lifting applied to each parcel is defined as

$$z_{lift,\,LAM}(z_i) = \begin{cases} z_i + h_m\left(1 - \dfrac{2z_i}{l_z}\right) & \text{for } z_i \leq l_z/2, \\ z_i & \text{for } z_i > l_z/2, \end{cases} \tag{12}$$

which decreases linearly with z_i from h_m at the surface to zero at a height equal to half the wavelength of a dry, linear, hydrostatic and steady mountain wave ($l_z/2 = \pi U/N_d$). This height represents the lowest level at which a streamline of a dry, linear, hydrostatic and steady mountain wave undergoes no upward displacement prior to its descent on the downwind side of the mountain wave. For the values of U and N_d used here, $l_z/2 = 4.7\,\mathrm{km}$, which corresponds well to the simulations (e.g. Figure 1(a)). As the majority of atmospheric moisture is contained at lower

© 2013 The Authors. *Quarterly Journal of the Royal Meteorological Society* published by John Wiley & Sons Ltd on behalf of the Royal Meteorological Society.

levels, only lifting below $l_z/2$ is considered. Such a simplified lifting profile clearly cannot faithfully represent the true three-dimensional dynamics of mountain waves. Nevertheless, as we will see in section 3.3, this approximation provides relatively accurate bulk condensation estimates.

The condensation rate can be written as

$$\mathbb{C}_{\mathrm{LAM}} = -\int_0^{l_z/2}\int_{-\infty}^{x_{\mathrm{lift,\ LAM}}} \frac{\mathrm{d}\rho_{\mathrm{v}}[z_{\mathrm{i}},\ z_{\mathrm{l}}(z_{\mathrm{i}},x)]}{\mathrm{d}t}\,\mathrm{d}x\,\mathrm{d}z_{\mathrm{i}}, \qquad (13)$$

where the parcel water vapour density, ρ_{v}, is written as a function of the level at which it originated, z_{i}, and the height along the assumed (2D) trajectory, $z_{\mathrm{l}}(z_{\mathrm{i}},x)$. The final x position to which the parcel is lifted is $x_{\mathrm{lift,\ LAM}}$ and so the inner integral limits correspond to the points $z_{\mathrm{l}}(z_{\mathrm{i}},-\infty)\equiv z_{\mathrm{i}}$ and $z_{\mathrm{l}}(z_{\mathrm{i}},x_{\mathrm{lift,\ LAM}})\equiv z_{\mathrm{lift,\ LAM}}(z_{\mathrm{i}})$, respectively. Given that $\mathrm{d}x\,\mathrm{d}\rho_{\mathrm{v}}/\mathrm{d}t \approx U\,\mathrm{d}z_{\mathrm{l}}\,\mathrm{d}\rho_{\mathrm{v}}/\mathrm{d}z_{\mathrm{l}}$, Eq. (13) can be written as

$$\mathbb{C}_{\mathrm{LAM}} = -U\int_0^{l_z/2}\int_{z_{\mathrm{i}}}^{z_{\mathrm{lift,\ LAM}}} \frac{\mathrm{d}\rho_{\mathrm{v}}(z_{\mathrm{i}},z_{\mathrm{l}})}{\mathrm{d}z_{\mathrm{l}}}\,\mathrm{d}z_{\mathrm{l}}\,\mathrm{d}z_{\mathrm{i}}, \qquad (14)$$

where, below the LCL, $\mathrm{d}\rho_{\mathrm{v}}/\mathrm{d}z_{\mathrm{l}}=0$ and the unsaturated potential temperature remains constant. Above the LCL, the parcel is lifted moist adiabatically and $\rho_{\mathrm{v}}=\rho_{\mathrm{vs}}$, the saturated water vapour density. Note that, given proper substitution for $z_{\mathrm{lift,\ LAM}}$, Eq. (14) is a general statement for any lifting mechanism and will be reused in section 3.4 to calculate the condensation rate for air lifted convectively. Evaluation of the inner integral in Eq. (14) yields the total condensation rate associated with a parcel originating at z_{i} and ascending to $z_{\mathrm{lift,\ LAM}}$ (a Lagrangian perspective), whereas evaluation of the outer integral yields the total condensation rate at $z=z_{\mathrm{l}}$ due to all parcels that are lifted through that layer (a Eulerian perspective). As the Eulerian form of the equation allows condensation rates to be calculated over different vertical layers, it will be utilized in section 3.2 to define separate condensation rates above and below the freezing level.

As in the simulations, the water vapour influx is computed from the upstream sounding as

$$\mathbb{I} = U\int_0^{z_{\mathrm{t}}} \rho_{\mathrm{v}}\,\mathrm{d}z, \qquad (15)$$

and so $\mathbb{CR}$ for a purely mechanically lifted flow can be calculated as $\mathbb{CR}_{\mathrm{LAM}}=\mathbb{C}_{\mathrm{LAM}}/\mathbb{I}$, where $\mathbb{C}_{\mathrm{LAM}}$ is found by inserting Eq. (12) into Eq. (14).

3.2. *Precipitation efficiency for purely mechanically lifted flow*

Early orographic precipitation models (Sawyer, 1956; Smith, 1979) assumed that all cloud condensate was instantly removed as precipitation. Not surprisingly, this assumption tends to overestimate the precipitation rate, as clouds are generally not perfectly efficient (Hobbs *et al.*, 1973). To improve upon this assumption, more recent studies have utilized linear precipitation efficiency models that assume constant formation and sedimentation time-scales as the condensate is advected over the mountain (Jiang and Smith, 2003; Smith and Barstad, 2004). In such models, the (linear) formation efficiency is

$$FE_{\mathrm{linear}} = \left(1+\frac{\tau_{\mathrm{form}}}{\tau_{\mathrm{a}}}\right)^{-1}, \qquad (16)$$

where τ_{form} is a constant formation time-scale (Jiang and Smith, 2003). Nonetheless, Cannon *et al.* (2012) showed that this formulation is incapable of reproducing the large differences in *FE* seen in stratiform orographic clouds like those in the LAM simulations. Consider for example the case of warm, nearly saturated air traversing a short but wide mountain. As τ_{a} contains only a weak dependence on the mountain height (and the corresponding condensation rate), it will predict a large FE_{linear} as $\tau_{\mathrm{a}} \gg \tau_{\mathrm{form}}$. In reality, however, no precipitation would form as there would be too little condensate to initiate precipitation formation (especially in liquid-only clouds that cannot grow snow via vapour deposition). In this situation, only a nonlinear formulation (where τ_{form} is a function of the condensation rate) can reproduce a realistic formation efficiency. Observational studies such as that of Smith *et al.* (2005) and numerical modelling studies such as that of Jiang and Smith (2003) have also cast doubt on the suitability of Eq. (16) for purely mechanically lifted orographic flows.

Here, the condensate generated by purely mechanical lifting is input into a 'box model' for precipitation efficiency. As shown in Figure 4, the model consists of 'frozen' and 'liquid' layers, which are defined above and below the freezing level, z_{f} (the values of z_{f} for different T_{s} are given in Table 1). The proportion of $\mathbb{C}_{\mathrm{LAM}}$ occurring in the frozen and liquid layers ($\mathbb{C}_{\mathrm{f}}$ and $\mathbb{C}_{\mathrm{l}}$, respectively) is estimated by switching the order of the integrals in Eq. (14) (the Eulerian approach) and altering the integrand limits so that

$$\mathbb{C}_{\mathrm{f}} = -U\int_{z_{\mathrm{f}}}^{l_z/2}\int_0^{z_{\mathrm{l}}} \frac{\mathrm{d}\rho_{\mathrm{v}}(z_{\mathrm{i}},\ z_{\mathrm{l}})}{\mathrm{d}z_{\mathrm{l}}}\,\mathrm{d}z_{\mathrm{i}}\,\mathrm{d}z_{\mathrm{l}}, \qquad (17)$$

$$\mathbb{C}_{\mathrm{l}} = -U\int_0^{z_{\mathrm{f}}}\int_0^{z_{\mathrm{l}}} \frac{\mathrm{d}\rho_{\mathrm{v}}(z_{\mathrm{i}},\ z_{\mathrm{l}})}{\mathrm{d}z_{\mathrm{l}}}\,\mathrm{d}z_{\mathrm{i}}\,\mathrm{d}z_{\mathrm{l}}, \qquad (18)$$

which states that the condensation rate at any level is equal to the sum of the local condensation rate of all parcels that rise through that level (i.e. for $0\le z_{\mathrm{i}}\le z_{\mathrm{l}}$). The total condensation rate in each layer is then found by integrating over all levels between $z_{\mathrm{f}}\le z_{\mathrm{l}}\le l_z/2$ (for the frozen layer), or $0\le z_{\mathrm{l}}\le z_{\mathrm{f}}$ (for the liquid layer). The sum of $\mathbb{C}_{\mathrm{f}}$ and $\mathbb{C}_{\mathrm{l}}$ is always equal to $\mathbb{C}_{\mathrm{LAM}}$.

For simplicity, all condensate in the box model is initially treated as liquid and is converted to snow in the frozen layer or rain in the liquid layer (graupel is not included). Rather than assume a linear formation rate (which is independent of $\mathbb{C}_{\mathrm{f}}$ or $\mathbb{C}_{\mathrm{l}}$), we propose a new nonlinear formation rate, $\mathbb{F}_{\mathrm{LAM}}$, which is equal to the sum of the dominant 'partial' formation rates found in the simulations. The partial formation rates considered in the frozen layer are vapour deposition to snow, $\mathbb{VDEP}$, and the accretion of supercooled cloud water by snow, $\mathbb{ACC}$. For simplicity, riming is not considered here (though it could be easily added). Note that $\mathbb{VDEP}$ is approximated as a pathway from supercooled liquid condensate to snow, via an instantaneous conversion to water vapour through the Bergeron mechanism (e.g. Rogers and Yau, 1989). In the liquid layer, the partial formation rates considered are the autoconversion rate of cloud water to rain ($\mathbb{AUT}$) and the collision and coalescence of cloud water and rain drops ($\mathbb{COCO}$). Therefore,

$$\mathbb{FE}_{\mathrm{LAM}} = \frac{\mathbb{F}_{\mathrm{LAM}}}{\mathbb{C}_{\mathrm{LAM}}} = \frac{\mathbb{VDEP}+\mathbb{ACC}+\mathbb{AUT}+\mathbb{COCO}}{\mathbb{C}_{\mathrm{LAM}}}. \qquad (19)$$

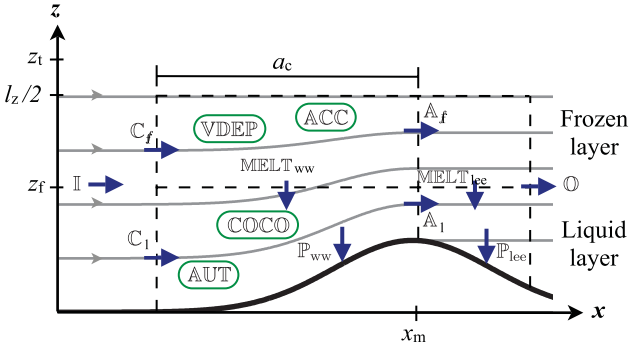

Figure 4. An overview of the precipitation efficiency box model developed for purely mechanically lifted flows. Symbols are as defined in the text. This figure is available in colour online at wileyonlinelibrary.com/journal/qj

© 2013 The Authors. *Quarterly Journal of the Royal Meteorological Society* published by John Wiley & Sons Ltd on behalf of the Royal Meteorological Society.

In addition, as depicted in Figure 4, snow melts to form rain upon reaching the liquid layer ($\mathbb{MELT}_{ww}$). Any remaining snow advected to the lee ($\mathbb{A}_f$) either melts to the liquid layer ($\mathbb{MELT}_{lee}$) or evaporates downstream. Rain forms in the liquid layer via autoconversion of cloud water ($\mathbb{AUT}$) or via collision and coalescence ($\mathbb{COCO}$). Rain that does not reach the surface on the windward slope ($\mathbb{P}_{ww,\,LAM}$) is advected to the lee ($\mathbb{A}_l$), where it either sediments to the surface ($\mathbb{P}_{lee,\,LAM}$) or is evaporated downstream. No precipitation formation is permitted in the lee. For completeness, the influx ($\mathbb{I}$) and outflux ($\mathbb{O}$) of water vapour are also shown in Figure 4. The derivation of these partial formation rates is provided in Appendix A, along with a discussion of the sensitivity of Eq. (19) to both uncertain constants and the lifting assumption defined in Eq. (12).

The total precipitation rate for a purely mechanically lifted flow is $\mathbb{P}_{LAM} = \mathbb{P}_{ww,\,LAM} + \mathbb{P}_{lee,\,LAM}$. The windward contribution is calculated as the rate at which rain sediments to the surface ($M_r/\tau_{r,\,sed}$ in the notation of Appendix A), which from Eqs (A2) and (A5) (in Appendix A) is

$$\mathbb{P}_{ww,\,LAM} = \frac{\mathbb{VDEP} + \mathbb{ACC}}{\left(1 + \frac{\tau_{melt}}{\tau_a}\right)\left(1 + \frac{\tau_{r,\,sed}}{\tau_a}\right)} + \frac{\mathbb{AUT} + \mathbb{COCO}}{\left(1 + \frac{\tau_{r,\,sed}}{\tau_a}\right)}. \tag{20}$$

The first term in Eq. (20) represents the rate at which snow forms (through $\mathbb{VDEP}$ or $\mathbb{ACC}$), melts to the liquid layer (in time τ_{melt}) and sediments to the surface (in time $\tau_{r,\,sed}$), and the second represents the rate at which rain forms (through $\mathbb{AUT}$ or $\mathbb{COCO}$) and sediments to the surface (in time $\tau_{r,\,sed}$). To determine $\mathbb{P}_{lee,\,LAM}$ we need to estimate the proportion of precipitation that does not evaporate once it is advected into the unsaturated environment in the lee of the mountain. For simplicity, we assume this evaporation occurs linearly, with a constant time-scale ($\tau_e = 500\,s$) and apply the same method to find

$$\mathbb{P}_{lee,\,LAM} = \frac{\mathbb{VDEP} + \mathbb{ACC}}{\left(1 + \frac{\tau_a}{\tau_{melt}}\right)\left(1 + \frac{\tau_{sn,\,sed}}{\tau_e}\right)} + \frac{\mathbb{VDEP} + \mathbb{ACC}}{\left(1 + \frac{\tau_{melt}}{\tau_a}\right)\left(1 + \frac{\tau_a}{\tau_{r,\,sed}}\right)\left(1 + \frac{\tau_{r,\,sed}}{\tau_e}\right)} + \frac{\mathbb{AUT} + \mathbb{COCO}}{\left(1 + \frac{\tau_a}{\tau_{r,\,sed}}\right)\left(1 + \frac{\tau_{r,\,sed}}{\tau_e}\right)}, \tag{21}$$

where

$$\tau_{sn,\,sed} = \frac{(z_{sn} - z_f)}{v_{sn}} + \frac{z_f}{v_r} \tag{22}$$

is the time taken for snow to sediment to the liquid layer and fall as rain to the surface (see Appendix A for definitions of the snow formation height, z_{sn}, and fall velocities of snow and rain, v_{sn} and v_r). The first term in Eq. (21) thus represents the rate at which snow is advected to the lee and sediments to the surface (via instantaneous melting at z_f), whilst the second term represents the rate at which snow melts to form rain in the liquid layer, is advected to the lee and then sediments to the surface. The final term in Eq. (21) represents the rate at which rain forms in the liquid layer, is advected to the lee and sediments to the surface. Note that the terms involving liquid (frozen) precipitation formation in Eqs (19)–(21) tend to zero as $z_f \to 0$ ($z_f \to l_z/2$), which implies that no rain occurs if the freezing level is too low and no snow occurs if the freezing level is too high. Given that the total precipitation rate for a purely mechanically lifted flow is $\mathbb{P}_{LAM} = \mathbb{P}_{ww,\,LAM} + \mathbb{P}_{lee,\,LAM}$, the sedimentation and precipitation efficiencies are simply $\mathbb{SE}_{LAM} = \mathbb{P}_{LAM}/\mathbb{F}_{LAM}$ and $\mathbb{PE}_{LAM} = \mathbb{P}_{LAM}/\mathbb{C}_{LAM} = \mathbb{FE}_{LAM} \times \mathbb{SE}_{LAM}$.

3.3. *Comparison with LAM simulations*

Figure 5 shows a comparison between the analytically predicted condensation ratio, precipitation efficiency and drying ratio for a purely mechanically lifted flow ($\mathbb{DR}_{LAM} = \mathbb{P}_{LAM}/\mathbb{I} = \mathbb{CR}_{LAM} \times \mathbb{PE}_{LAM}$) and those obtained from the laminar simulations. In almost all cases, the model slightly overestimates $\mathbb{CR}_{LAM}$. This could be due to the effect of surface drag, which is neglected in Eq. (12) but present in the simulations, or to assumptions concerning the vertical lifting profile. As discussed in Kirshbaum and Smith (2008) and Cannon *et al.* (2012), the tendency for the condensation ratio to decrease with T_s is a consequence of greater latent heat release and larger moisture scale heights in warmer environments. In many cases (most notably in Figure 5(c)), there is a cancellation of errors between the slightly overpredicted $\mathbb{CR}_{LAM}$ and slightly underpredicted $\mathbb{PE}_{LAM}$, resulting in close agreement between $\mathbb{DR}_{LAM}$ and DR_{LAM}.

To understand the trends in $\mathbb{PE}_{LAM}$, we must first consider the ability of the analytical model to reproduce the simulated formation and sedimentation efficiencies. In Cannon *et al.* (2012), a subset of LAM simulations (a15-h1 and a60-h2 only) was performed in which the partial precipitation formation rates through several important mechanisms were calculated. In Table 2, we compare these simulation results with those predicted by the analytical model. To enable a direct comparison, the individual formation rates from the analytical model are recast into autoconversion, collection and deposition efficiencies. The autoconversion efficiency is defined as $\mathbb{AC} = \mathbb{AUT}/\mathbb{C}_{LAM}$ and represents the proportion of condensate that is converted to rain via the autoconversion of cloud water. The collection efficiency, $\mathbb{COL} = (\mathbb{ACC} + \mathbb{COCO})/\mathbb{C}_{LAM}$, is the proportion of condensate converted to precipitation through either accretion in the frozen layer or collision and coalescence in the liquid layer. Finally, the deposition efficiency, $\mathbb{DEP} = \mathbb{VDEP}/\mathbb{C}_{LAM}$, is the proportion of condensate converted to snow via vapour deposition. The total formation efficiency for the analytical model is therefore $\mathbb{FE}_{LAM} = \mathbb{AC} + \mathbb{COL} + \mathbb{DEP}$. For reference, the linear formulation (Eq. (16) with $\tau_{form} = 1000\,s$) is also shown.

In the a15-h1-LAM simulations, there is scant vapour deposition in all but the coldest cases, leaving collection as the primary mechanism for precipitation formation (Table 2). This occurs because vapour deposition is suppressed by a short advection time, a small supply of condensate and a weak supersaturation with respect to ice. Rain formation therefore dominates over snow formation, even in the coldest a15-h1-LAM simulations. As T_s increases, so does the dominant warm-rain formation mechanism (collision and coalescence) and so FE_{LAM} increases. In contrast, the analytical model overpredicts $\mathbb{DEP}$ slightly for the a15-h1-T277 case and a significant amount of snow forms in the frozen layer. In contrast to the simulations, the total collection rate ($\mathbb{COL} = \mathbb{COCO} + \mathbb{ACC}$) decreases slightly at low to intermediate T_s before increasing at intermediate to high T_s. This occurs because the majority of collection at low T_s occurs via $\mathbb{ACC}$ in the frozen layer, which decreases as T_s rises and the depth of the frozen layer decreases (not shown). At high T_s, most collection occurs through $\mathbb{COCO}$ in the liquid layer (not shown) and so $\mathbb{FE}_{LAM}$ increases.

The advection time-scale and lifting amplitude are larger in the a60-h2 cases. This leads to colder average cloud temperatures and a greater proportion of the total condensate occurring in the frozen layer, enhancing $\mathbb{DEP}$ and $\mathbb{ACC}$ (Table 2). This directly enhances $\mathbb{COL}$ in the frozen layer and indirectly enhances $\mathbb{COL}$ in the liquid layer by seeding it with snow (thus increasing

© 2013 The Authors. *Quarterly Journal of the Royal Meteorological Society* published by John Wiley & Sons Ltd on behalf of the Royal Meteorological Society.

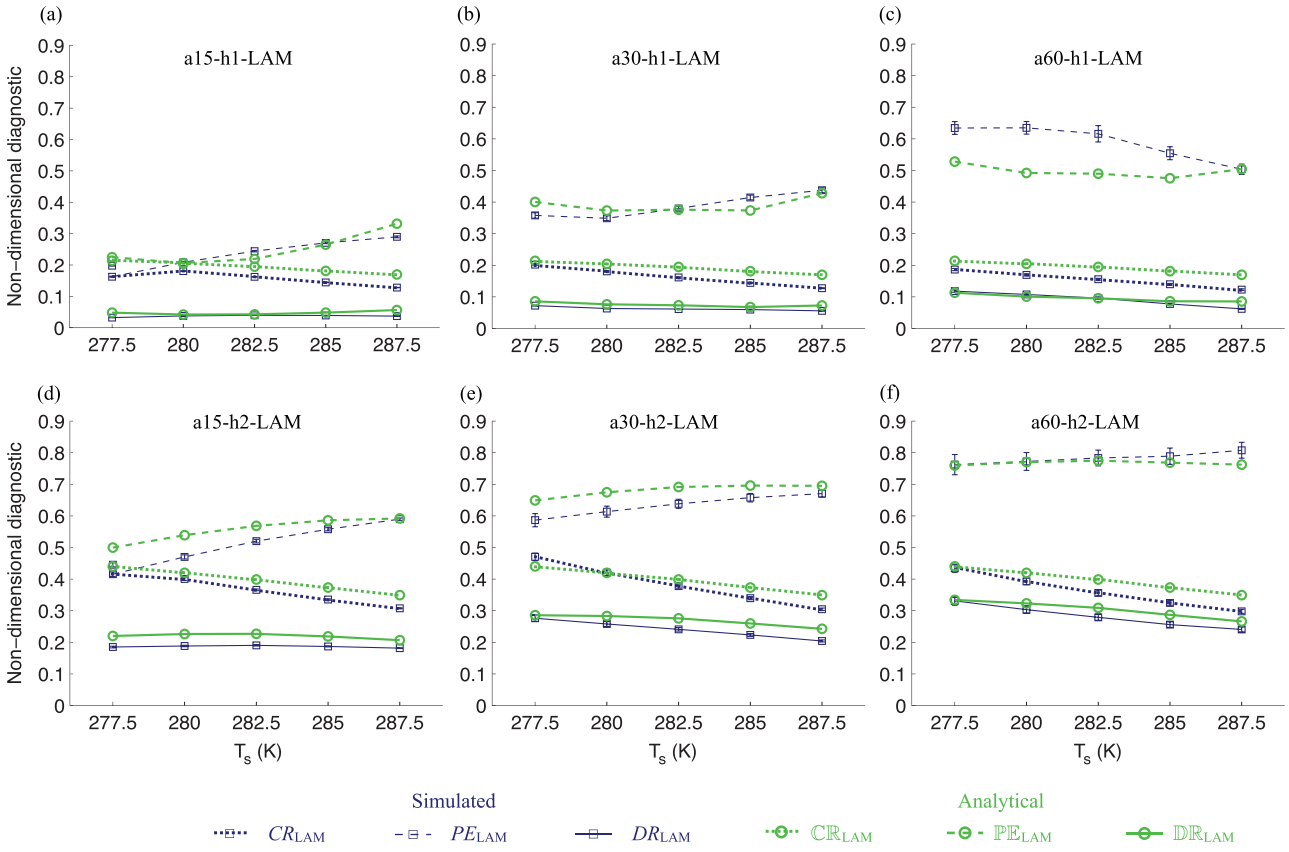

Figure 5. Simulated (black, blue online) and analytically derived (grey, green online) non-dimensional diagnostics for purely mechanically lifted (laminar) flow. Shown are the cases (a) a15-h1, (b) a30-h1, (c) a60-h1, (d) a15-h2, (e) a30-h2 and (f) a60-h2. For all panels, CR_{LAM} and $\mathbb{CR}_{\mathrm{LAM}}$ are dotted, PE_{LAM} and $\mathbb{PE}_{\mathrm{LAM}}$ are dashed and DR_{LAM} and $\mathbb{DR}_{\mathrm{LAM}}$ are solid. The error bars on the simulation diagnostics represent the standard error of the spatially averaged, time-varying diagnostics. The size of these bars generally increases in flows with increased convective vigour and when the model dimensionality or resolution is decreased. This figure is available in colour online at wileyonlinelibrary.com/journal/qj

Table 2. Partial (and total) laminar formation efficiencies for various simulations (standard font) compared with values predicted by the analytical model ('blackboard bold' font). The linear formation efficiency predicted by (16) is also shown. In addition, the laminar sedimentation efficiencies predicted by the analytical model are also compared to the simulations. See text for definitions.

Case	AC / $\mathbb{AC}$	COL / $\mathbb{COL}$	DEP / $\mathbb{DEP}$	FE_{LAM} / $\mathbb{FE}_{\mathrm{LAM}}$	FE_{linear}	SE_{LAM} / $\mathbb{SE}_{\mathrm{LAM}}$
a15-h1-LAM-T277	0.03/0.00	0.15/0.26	0.01/0.04	0.19/0.30	0.56	0.87/ 0.76
a15-h1-LAM-T282	0.03/0.00	0.24/0.23	0.00/0.01	0.27/ 0.24	0.56	0.89/0.92
a15-h1-LAM-T287	0.03/0.00	0.29/0.35	0.00/0.00	0.33/0.35	0.53	0.88/0.94
a60-h2-LAM-T277	0.02/0.00	0.47/0.66	0.40/0.20	0.89/ 0.86	0.86	0.86/0.88
a60-h2-LAM-T282	0.02/0.00	0.63/0.72	0.24/0.12	0.89/0.84	0.86	0.88/0.93
a60-h2-LAM-T287	0.02/0.00	0.76/0.75	0.09/0.04	0.87/0.79	0.85	0.92/0.96

$\mathbb{COCO}$). As in the simulations, $\mathbb{COL}$ increases with T_s for a tall and wide mountain, but this is offset by the decrease in $\mathbb{DEP}$, leaving a small overall decrease in $\mathbb{FE}_{\mathrm{LAM}}$. The analytical model overpredicts $\mathbb{COL}$ in the cold cases, but this is largely offset by an underprediction in $\mathbb{DEP}$ by around a factor of two (for all T_s). Whilst the agreement in $\mathbb{FE}_{\mathrm{LAM}}$ with the simulations is therefore good at $T_s = 277.5$ K, the analytical model produces a slightly larger decrease with T_s than was simulated. For the cases in Table 2, $\mathbb{AC}$ does not contribute to $\mathbb{FE}_{\mathrm{LAM}}$, whereas in the simulations AC is small but non-zero.

As predicted at the beginning of section 3.2, whilst a linear formation efficiency (Eq. (16)) can be tuned to agree well with some of the simulation results, it cannot reproduce the wide range of formation efficiencies found throughout the parameter space considered (Table 2). The linear formulation contains no knowledge of the underlying formation mechanisms and so cannot reproduce the dependence on mountain height or the sharp enhancement of formation efficiency with temperature over low and narrow mountains. Although it does not perfectly match the simulation results, the analytical model developed here shows much better quantitative agreement (for both magnitudes and sensitivities) than the linear formulation.

Also shown in Table 2 is a comparison between the simulated sedimentation efficiencies and those predicted by the analytical model. The high simulated sedimentation efficiencies ($SE_{\mathrm{LAM}} > 0.8$) are reproduced well in most cases. As mentioned previously, the analytical model tends to overpredict the proportion of precipitation forming as snow for cold flows. This induces an underprediction in $\mathbb{SE}_{\mathrm{LAM}}$ over the narrowest mountains, where less of the slowly falling snow reaches the ground before reaching the lee. In most cases, the small errors in $\mathbb{FE}_{\mathrm{LAM}}$ relative to the simulations cancel at least partially with small errors in $\mathbb{SE}_{\mathrm{LAM}}$ to produce closer agreement in $\mathbb{PE}_{\mathrm{LAM}}$.

3.4. *Condensation ratio for convection-permitting flow*

A purely convective flow is one in which the forced lifting is sufficient to readily initiate convection (i.e. $\tau_{\mathrm{LFC}} << \tau_{\mathrm{LAM1}}$) and the time-scale for convective overturning is much shorter than the advective time-scale (i.e. $\tau_{\mathrm{CONV}} << \tau_{\mathrm{LAM2}}$). The amount of

© 2013 The Authors. *Quarterly Journal of the Royal Meteorological Society* published by John Wiley & Sons Ltd on behalf of the Royal Meteorological Society.

lifting for such a flow is estimated as

$$z_{\text{lift, CONV}}(z_\text{i}) = \begin{cases} z_{\text{LNB}}(z_\text{i}) + h_\text{m}\left(1 - \dfrac{2z_\text{i}}{l_z}\right) \\ \quad \text{for } z_{\text{lift, LAM}}(z_\text{i}) \geq z_{\text{LFC}}(z_\text{i}), \\ \\ z_{\text{lift, LAM}}(z_\text{i}) \\ \quad \text{for } z_{\text{lift, LAM}}(z_\text{i}) < z_{\text{LFC}}(z_\text{i}), \end{cases} \tag{23}$$

where air that has positive CAPE and is raised to its LFC experiences buoyant lifting (to its LNB) in addition to the mountain-scale mechanical lifting, whereas air that is not raised to its LFC experiences only mechanical lifting (as in Eq. (12)). Note that z_{LFC} and z_{LNB} are calculated for each level separately and are thus functions of z_i. The condensation ratio for a purely convective flow is $\mathbb{CR}_{\text{CONV}} = \mathbb{C}_{\text{CONV}}/\mathbb{I}$, where $\mathbb{C}_{\text{CONV}}$ is found by substituting $z_{\text{lift, LAM}}$ for $z_{\text{lift, CONV}}$ in Eq. (14).

Utilizing the weighting functions α_{CONV} and α_{LAM}, developed at the beginning of section 3, the total condensation ratio for convection-permitting flow is

$$\mathbb{CR}_{\text{CP}} = \frac{\alpha_{\text{LAM}}\mathbb{C}_{\text{LAM}} + \alpha_{\text{CONV}}\mathbb{C}_{\text{CONV}}}{\mathbb{I}}. \tag{24}$$

3.5. *Precipitation efficiency for convection-permitting flow*

Convective clouds are generally efficient at forming precipitation because their air parcels tend to undergo large vertical displacements and generate large amounts of cloud condensate. Consequently, flows for which the advective time-scale is long enough for convection to form may not suffer the same inefficiencies in precipitation formation as observed in some of the LAM simulations, diminishing the need for a complex (nonlinear) formulation. Therefore, for simplicity, Eq. (16) is used to describe the efficiency with which precipitation is formed from the available cloud condensate. The formation time-scale used, $\tau_{\text{form, CONV}} = 1000$ s, is a commonly used value in convection parametrizations such as the Kain–Fritsch scheme (Kain and Fritsch, 1990, 1993; Kain, 2004).

As shown schematically in Figure 6, the precipitation formation rate for a convective flow is also critically dependent on the rate of convectively induced cloud evaporation, which reduces the amount of condensate available for conversion to precipitation in convective updraughts (Kirshbaum and Smith, 2008; Cannon *et al.*, 2012). Whilst in general convective precipitation may also evaporate, analysis from the 2D CP simulations in Cannon *et al.* (2012) (which output a large number of microphysical conversion rates) suggests that the precipitation evaporation rate is small for the very humid cases considered here. Convectively induced evaporation is included in the convective formation efficiency through simple models for the evaporation occurring via compensating subsidence ($\mathbb{SUB}$) and the detrainment of cloudy air (to represent environmental mixing) ($\mathbb{DET}$). The formation efficiency of a convective flow is therefore written as

$$\mathbb{FE}_{\text{CONV}} = \left(1 - \frac{\mathbb{SUB}}{\mathbb{C}_{\text{CONV}}} - \frac{\mathbb{DET}}{\mathbb{C}_{\text{CONV}}}\right)\left(1 + \frac{\tau_{\text{form, CONV}}}{\tau_\text{a}}\right)^{-1}, \tag{25}$$

where the quantity in the first parentheses is the proportion of condensate that remains once evaporation takes place. This is multiplied by Eq. (16) to yield the overall formation efficiency.

As convective updraughts produce an upward mass flux relative to the mean orographically forced ascent, mass continuity demands that there also be a compensating mass flux downwards. Modern convection parametrizations account for this through negatively buoyant downdraughts and environmental subsidence. However, for simplicity we neglect downdraughts and use instead a simple adiabatic sorting model to predict the amount of subsidence needed to conserve overall mass. In Figure 7, an atmospheric profile with $T_\text{s} = 287.5$ K and $h_\text{m} = 2$ km is shown at different stages of the adiabatic sorting. In stage 1, conditional instability (levels with $CAPE > 0$) is present near the surface (not shown). Levels (with initial height z_i) for which the mechanically forced lifting prescribed by Eq. (12) exceeds $z_{\text{LFC}}(z_\text{i})$ are raised adiabatically to $z_{\text{lift, CONV}}(z_\text{i})$ (Eq. (23), stage 2). Note that this is the same lifting used to calculate the convective condensation rate in section 3.4. The amount of compensating subsidence is then calculated as

$$\mathbb{SUB} = U\int_0^{l_z/2}\left[\rho_\text{v}(z_\text{fin}) - \rho_\text{v}(z_{\text{lift, CONV}})\right]\,\text{d}z_\text{i}, \tag{26}$$

where

$$z_\text{fin} = \max\left[z_\text{SUB} + z_{\text{lift, LAM}}(z_\text{SUB}),\ z_\text{LCL}\right] \tag{27}$$

is the final position of the parcel after undergoing subsidence (stage 3). In Eq. (27), z_SUB is the level to which parcels would subside if not for the average mountain-scale ascent, $z_{\text{lift, LAM}}(z_\text{SUB})$. This is calculated using Eq. (12) but with proper substitution of z_SUB for z_i. Note that parcels initially above the maximum $z_{\text{lift, CONV}}$ remain unaffected by the reorganization

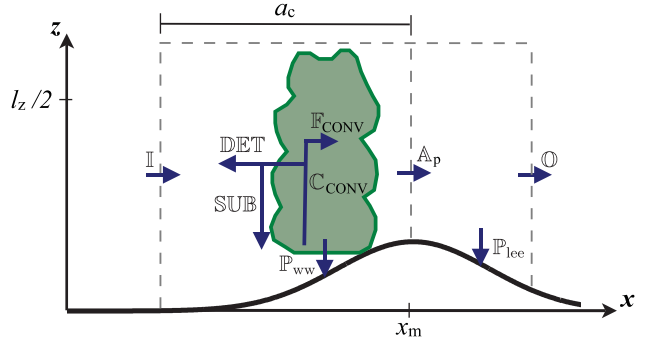

Figure 6. An overview of the formulation developed for purely convective flows. Symbols are as defined in the text. This figure is available in colour online at wileyonlinelibrary.com/journal/qj

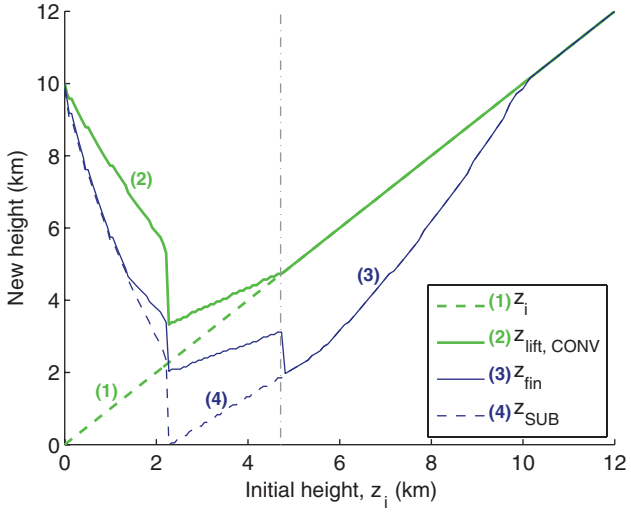

Figure 7. An atmospheric profile with $T_\text{s} = 287.5$ K undergoing adiabatic lifting and subsidence over a mountain with $h_\text{m} = 2$ km in stages. Stage 1 is defined by the initial atmospheric profile (dashed grey, green online), which is lifted according to Eq. (23) (solid grey, green online) in stage 2. In stage 3, the air subsides to the level prescribed by Eq. (27) (solid black, blue online) and stage 4 indicates the level to which the profile would subside without adjustment for orographically forced ascent, z_SUB (dashed black, blue online). The height at which the direct orographic lifting reduces to zero ($z_\text{i} = l_z/2$) is shown as a grey, vertical, dot–dashed line. This figure is available in colour online at wileyonlinelibrary.com/journal/qj

© 2013 The Authors. *Quarterly Journal of the Royal Meteorological Society* published by John Wiley & Sons Ltd on behalf of the Royal Meteorological Society.

below (and may also be high enough to escape orographic lifting). To exclude unsaturated descent, no descent below z_{LCL} contributes to $\mathbb{SUB}$. For completeness, the profile of z_{SUB} is shown as stage 4 in Figure 7.

The detrainment of condensate from the cloud to the environment is estimated as

$$\mathbb{DET} = \int_0^{l_z/2} w_{CONV} \left[\rho_v(z_i) - \rho_v(z_{lift,\,CONV})\right] \mathrm{d}z_i. \qquad (28)$$

The term in the square brackets represents the total amount of condensate produced when a parcel is lifted adiabatically from its initial height z_i to $z_{lift,\,CONV}$. This is equal to the total change in condensate between the parcel and the environment throughout the ascent (assuming the environment surrounding the updraught is unsaturated and that no condensate is lost as the parcel rises). Multiplying this value by the characteristic updraught velocity, $w_{CONV} = \gamma\sqrt{CAPE}$, thus provides an estimate for the total rate of detrainment of condensate to the environment for the ascent of that parcel. The total $\mathbb{DET}$ is determined by integrating over all vertical levels that experience convective lifting, from $z_i = 0$ to $z_i = l_z/2$.

As the thermodynamic properties of the parcel upon its ascent are calculated from adiabatic vertical displacements, this simple approach neglects the fact that in reality parcels also entrain air from the surrounding environment as they rise. Entrainment can significantly increase the vertical mass flux of the plume but it also decreases the updraught buoyancy through drying and evaporative cooling. Its overall impact on the net condensation rate is thus not immediately obvious. Although these competing effects may be estimated by entraining plume models (Kain and Fritsch, 1990), such a detailed treatment is avoided here for simplicity. Instead, the updraught ascent is treated as adiabatic (with constant equivalent potential temperature) and all environmental mixing occurs as detrainment.

The formation efficiency for a convection-permitting flow is

$$\begin{aligned}\mathbb{FE}_{CP} &= \frac{\alpha_{LAM}\mathbb{F}_{LAM} + \alpha_{CONV}\mathbb{F}_{CONV}}{\alpha_{LAM}\mathbb{C}_{LAM} + \alpha_{CONV}\mathbb{C}_{CONV}} \\ &= \mathbb{FE}_{LAM}\left(\frac{\alpha_{LAM}\mathbb{CR}_{LAM}}{\mathbb{CR}_{CP}}\right) \\ &\quad + \mathbb{FE}_{CONV}\left(\frac{\alpha_{CONV}\mathbb{CR}_{CONV}}{\mathbb{CR}_{CP}}\right),\end{aligned} \qquad (29)$$

where $\mathbb{F}_{CONV} = \mathbb{FE}_{CONV} \times \mathbb{C}_{CONV}$ and, as for the derivation of $\mathbb{CR}_{CP}$ in (24), α_{LAM} and α_{CONV} (Eqs (10)–(11)) are again used to determine the proportions of condensate that are subject to purely mechanically forced and convective processes.

The sedimentation efficiency for a purely convective flow is calculated using the same approach as in the $\mathbb{PE}_{LAM}$ formulation (section 3.2). As there, we assume a linear process using a time-scale for sedimentation, which in this case is estimated as $\tau_{sed,\,CONV} = z_p/v_p$, where z_p is the mean height at which precipitation is formed and $v_p = 5\,\mathrm{m\,s^{-1}}$ is a constant precipitation fall speed (assumed equal to the fall speed of rain in Appendix A). z_p is approximated as a condensate-weighted average above the surface. Whilst significant graupel is also formed in the CP simulations and can fall faster than rain (Thompson *et al.*, 2008), for simplicity it is neglected here. The precipitation rate for a purely convective flow is therefore

$$\begin{aligned}\mathbb{P}_{CONV} &= \frac{\mathbb{F}_{CONV}}{\left(1 + \frac{\tau_{sed,\,CONV}}{\tau_a}\right)} \\ &\quad + \frac{\mathbb{F}_{CONV}}{\left(1 + \frac{\tau_a}{\tau_{sed,\,CONV}}\right)\left(1 + \frac{\tau_{sed,\,CONV}}{\tau_e}\right)},\end{aligned} \qquad (30)$$

where the first and second terms respectively represent the windward and leeward components of precipitation. For lee side precipitation evaporation, the same time-scale is used as for a purely mechanically lifted flow ($\tau_e = 500$ s).

Given these diagnostics, the sedimentation efficiency for a convection-permitting flow is

$$\begin{aligned}\mathbb{SE}_{CP} &= \frac{\alpha_{LAM}\mathbb{P}_{LAM} + \alpha_{CONV}\mathbb{P}_{CONV}}{\alpha_{LAM}\mathbb{F}_{LAM} + \alpha_{CONV}\mathbb{F}_{CONV}} \\ &= \mathbb{SE}_{LAM}\left(\frac{\alpha_{LAM}\mathbb{F}_{LAM}}{\alpha_{LAM}\mathbb{F}_{LAM} + \alpha_{CONV}\mathbb{F}_{CONV}}\right) \\ &\quad + \mathbb{SE}_{CONV}\left(\frac{\alpha_{CONV}\mathbb{F}_{CONV}}{\alpha_{LAM}\mathbb{F}_{LAM} + \alpha_{CONV}\mathbb{F}_{CONV}}\right),\end{aligned} \qquad (31)$$

where $\mathbb{SE}_{CONV} = \mathbb{P}_{CONV}/\mathbb{F}_{CONV}$. The precipitation efficiency for convection-permitting flow is

$$\begin{aligned}\mathbb{PE}_{CP} &= \mathbb{FE}_{CP} \times \mathbb{SE}_{CP} \\ &= \mathbb{PE}_{LAM}\left(\frac{\alpha_{LAM}\mathbb{CR}_{LAM}}{\mathbb{CR}_{CP}}\right) \\ &\quad + \mathbb{PE}_{CONV}\left(\frac{\alpha_{CONV}\mathbb{CR}_{CONV}}{\mathbb{CR}_{CP}}\right),\end{aligned} \qquad (32)$$

where $\mathbb{PE}_{CONV} = \mathbb{P}_{CONV}/\mathbb{C}_{CONV}$.

3.6. *Comparison with CP simulations*

Figure 8 shows a comparison between the analytically predicted condensation ratio, precipitation efficiency and drying ratio (which is simply calculated as $\mathbb{DR}_{CP} = \mathbb{P}_{CP}/\mathbb{I} = \mathbb{CR}_{CP} \times \mathbb{PE}_{CP}$) for a convection-permitting flow and results obtained from the simulations. As discussed in Cannon *et al.* (2012), the simulated CR_{CP} may be slightly underestimated due to the inability of the 1 km grid length simulations to resolve the kinetic and potential energy spectra of convective eddies fully; however, the basic sensitivities of the analytically derived $\mathbb{CR}_{CP}$ are in agreement with the simulations; it increases with h_m and (for high T_s when embedded convection is present) a_m and T_s. The main deficiency is that $\mathbb{CR}_{CP}$ is overpredicted relative to the simulations when convection is present but has little time to form and overturn (i.e. over short and narrow mountains at high T_s such as in Figure 8(a), (b) and d)).

Most of the trends in $\mathbb{PE}_{CP}$ (Figure 8) can be interpreted through the behaviour of $\mathbb{FE}_{CP}$ in different regions of parameter space. To investigate this, we used the 2D CP simulations of Cannon *et al.* (2012) (which output a large number of microphysical conversion rates) to evaluate the formation and upslope evaporation efficiencies predicted by the analytical model. Figure 9(a) and (b) compare the convectively induced upslope evaporation efficiency,

$$\mathbb{EE}_{cloud} = \frac{\alpha_{CONV}\left(\mathbb{SUB} + \mathbb{DET}\right)}{\alpha_{LAM}\mathbb{C}_{LAM} + \alpha_{CONV}\mathbb{C}_{CONV}}, \qquad (33)$$

with the upslope cloud evaporation efficiency from the a15-h1 and a60-h2 2D CP simulations, respectively. As discussed in Cannon *et al.* (2012), in simulations where significant convection developed, cloud evaporation due to gravity wave subsidence aloft contributed only a small amount to the total and the bulk of the cloud evaporation was convectively induced. Although $\mathbb{EE}_{cloud}$ agrees well with the 2D CP simulation in the a60-h2 case (Figure 9(b)), it overestimates substantially the low evaporation rates found in the a15-h1 case (Figure 9(a)). Note that the analytical model does not account for non-convective upslope evaporation and so it predicts zero upslope evaporation for a purely mechanically lifted flow (for clarity, these $\mathbb{EE}_{cloud} = 0$ lines are omitted from the figures). This assumption introduces a

© 2013 The Authors. *Quarterly Journal of the Royal Meteorological Society* published by John Wiley & Sons Ltd on behalf of the Royal Meteorological Society.

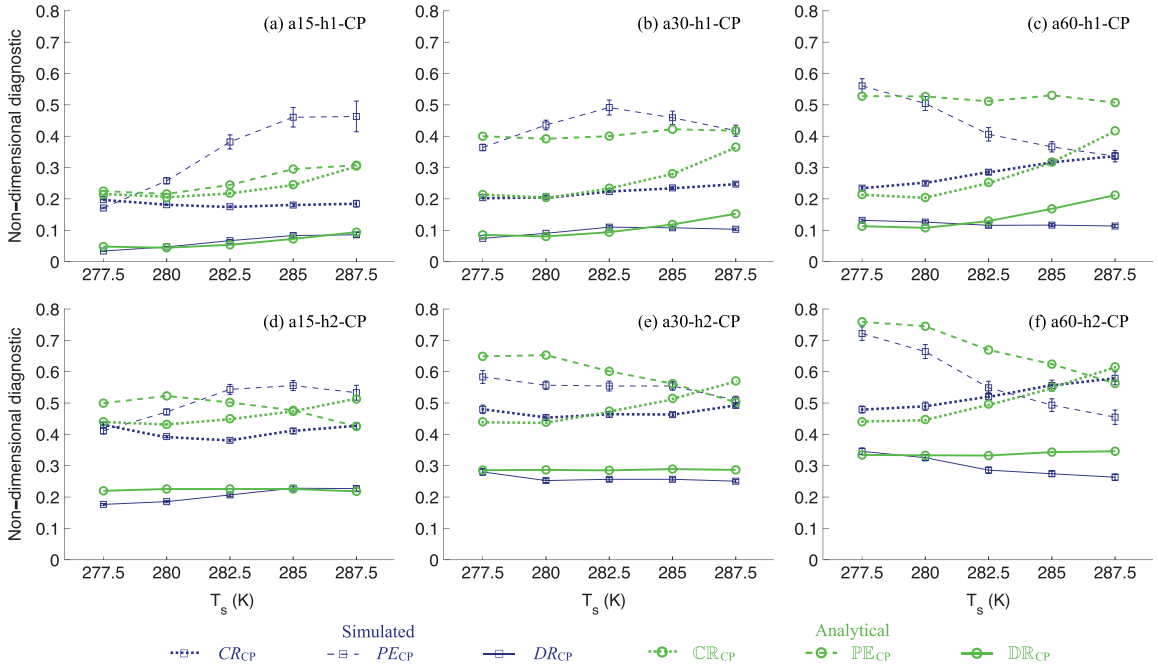

Figure 8. Simulated (black, blue online) and analytically derived (grey, green online) non-dimensional diagnostics for convection-permitting flow. Cases shown are (a) a15-h1, (b) a30-h1, (c) a60-h1, (d) a15-h2, (e) a30-h2 and (f) a60-h2. In each panel, CR_{CP} and $\mathbb{CR}_{CP}$ are dotted, PE_{CP} and $\mathbb{PE}_{CP}$ are dashed and DR_{CP} and $\mathbb{DR}_{CP}$ are solid. Error bars are as in Figure 5. This figure is available in colour online at wileyonlinelibrary.com/journal/qj

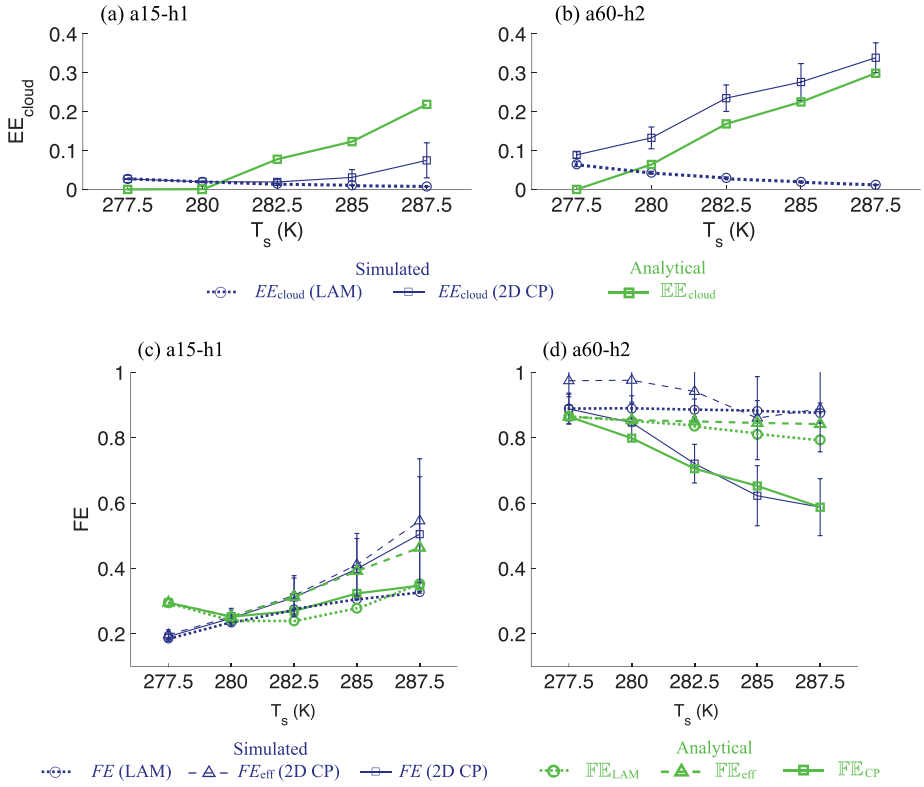

Figure 9. (a, b) The upslope cloud evaporation rate and (c, d) the precipitation formation efficiency for the a15-h1 and a60-h2 cases. Also shown in (c, d) is the effective formation efficiency (FE_{eff}). For all panels, the model-predicted diagnostics (grey, green online) as well as those of the LAM and 2D CP simulations (black, blue online) are plotted. Note that the analytical model neglects non-convective upslope evaporation and so predicts $\mathbb{EE}_{cloud} = 0$ for purely mechanically lifted flows (for clarity, these lines are neglected from panels (a) and (b)). Error bars are as in Figure 5. This figure is available in colour online at wileyonlinelibrary.com/journal/qj

small error at low T_s, particularly over wide and tall mountains where some cloud evaporation occurs aloft.

Figure 9(c) and (d) shows comparisons between $\mathbb{FE}_{LAM}$, $\mathbb{FE}_{CP}$ (Eqs (19) and (30)) and FE_{LAM} and FE_{CP} (from the 2D CP simulations) for the a15-h1 and a60-h2 cases, respectively. Also shown are the *effective* formation efficiencies, $\mathbb{FE}_{eff}$ and FE_{eff}, which represent the formation efficiency associated with the *available* condensate (i.e. that which does not evaporate). This is equivalent to replacing $\mathbb{C}_{CONV}$ with $\mathbb{C}_{CONV} - \mathbb{SUB} - \mathbb{DET}$ in Eq. (25). The decrease in formation efficiency with increasing T_s associated with convectively induced evaporation in the a60-h2 case is well reproduced by the analytical model (Figure 9(d)). As precipitation forms efficiently in this case even in the absence of embedded convection, $\mathbb{FE}_{eff}$ is only marginally enhanced relative to the equivalent values for a purely mechanically lifted flow. In contrast, $\mathbb{EE}_{cloud}$ is maximized in this region of parameter space and so there is a strong decrease in $\mathbb{FE}_{CP}$ when convection is present.

© 2013 The Authors. *Quarterly Journal of the Royal Meteorological Society* published by John Wiley & Sons Ltd on behalf of the Royal Meteorological Society.

In the a15-h1 case (Figure 9(c)), although embedded convection causes an enhancement of $\mathbb{FE}_{\text{eff}}$ at larger T_s, the overprediction of $\mathbb{EE}_{\text{cloud}}$ by the analytical model results in an underprediction of $\mathbb{FE}_{\text{CP}}$ relative to the simulations. Whilst three-dimensional, eddy-resolving CP simulations might predict higher cloud evaporation rates than observed in the 2D CP simulations, the sensitivity tests in Cannon *et al.* (2012) suggested that poor resolution in the simulations is unlikely to account fully for this overprediction. Physically, this underprediction at low a_m may be due to (i) the neglect of interactions between the mountain wave and convective mixing, where for narrow mountains the weaker upstream tilt of the mountain wave may lead to moister air aloft and reduced convective entrainment, and/or (ii) the lack of a dynamical enhancement of convective vigour over steeper slopes (Kirshbaum and Smith, 2009).

For narrow mountains (Figure 8(a) and (d)), the analytical model underpredicts $\mathbb{PE}_{\text{CP}}$ at high T_s when compared with the CP simulations, which is consistent with an overprediction of $\mathbb{EE}_{\text{cloud}}$. For wide mountains (Figure 8(c) and (f)), there is an overprediction of $\mathbb{PE}_{\text{CP}}$ at high T_s relative to the simulations. This may be due to a small overprediction of $\mathbb{SE}_{\text{CP}}$ rather than $\mathbb{FE}_{\text{CP}}$, which, at least for the a60-h2-CP case, was reproduced accurately when compared with the 2D CP simulations (Figure 9(d)).

The trends in $\mathbb{DR}_{\text{CP}}$ with a_m, h_m and in many cases T_s are well reproduced by the analytical model. For narrow mountains (Figure 8(a) and (d)), the overestimation of $\mathbb{CR}_{\text{CP}}$ at high T_s relative to the simulations is largely compensated for by the underestimation of $\mathbb{PE}_{\text{CP}}$. As the mountain width increases (Figure 8(c) and (f)), the small overestimation of $\mathbb{DR}_{\text{CP}}$ at high T_s is predominantly a consequence of overpredictions in $\mathbb{PE}_{\text{CP}}$.

3.7. *The enhancement due to embedded convection*

The central conclusion of Cannon *et al.* (2012) was that, whilst convective cells generate larger vertical air displacements and locally more condensate, this did not always lead to enhanced area-averaged precipitation. In flows that *cannot* create precipitation efficiently via stratiform processes alone (e.g. those over short, narrow mountains), they found that the enhanced condensation due to embedded convection results in enhanced precipitation formation and increased area-averaged precipitation. However, in flows that *can* create precipitation efficiently via stratiform processes (e.g. those over tall, wide mountains), they found that the enhanced condensation due to embedded convection is offset by increased cloud evaporation, yielding little net change in area-averaged precipitation. To assess whether the analytical model reproduces this effect, Figure 10 shows the enhancement (β) of $\Psi = CR, PE, DR, \mathbb{CR}, \mathbb{PE}$ or $\mathbb{DR}$ for different a_m, h_m and T_s. These enhancements are calculated as

$$\beta_\Psi = \left(\frac{\Psi_{\text{CP}} - \Psi_{\text{LAM}}}{\Psi_{\text{LAM}}} \right) \times 100\%. \tag{34}$$

Thus, $\beta = 100\%$ when the CP diagnostic is double that of the LAM diagnostic and 0% when there is no difference between them. Negative values correspond to a decrease due to embedded convection.

As in the simulations, the analytical model predicts smaller $\mathbb{DR}$ enhancements for the h2 cases than for the h1 cases, as the enhanced $\mathbb{CR}$ is largely offset by the reduced $\mathbb{PE}$. Whilst the strong increase in β_{CR} with a_m at high T_s is generally well reproduced by the analytical model, the decrease in β_{PE} with a_m is consistently underestimated (particularly over short mountains; Figure 10(a)–(c)). This leads to an *increase* in $\beta_{\mathbb{DR}}$ with a_m, as opposed to the decrease in β_{DR} with a_m found in the simulations. As discussed in section 3.6, the underprediction of $\mathbb{PE}_{\text{CP}}$ in the a15-h1 case can be attributed to an overprediction of $\mathbb{EE}_{\text{cloud}}$ (Figure 9(a) and (c)), whereas the overprediction in the a60-h1 case is predominantly due to an overprediction of $\mathbb{PE}_{\text{CP}}$ (Figure 8(c)).

4. Summary and conclusions

A new bulk (area-averaged) analytical model for mixed-phase orographic precipitation with embedded convection has been developed, which explains many sensitivities found in idealized, convection-permitting numerical simulations. To the authors'

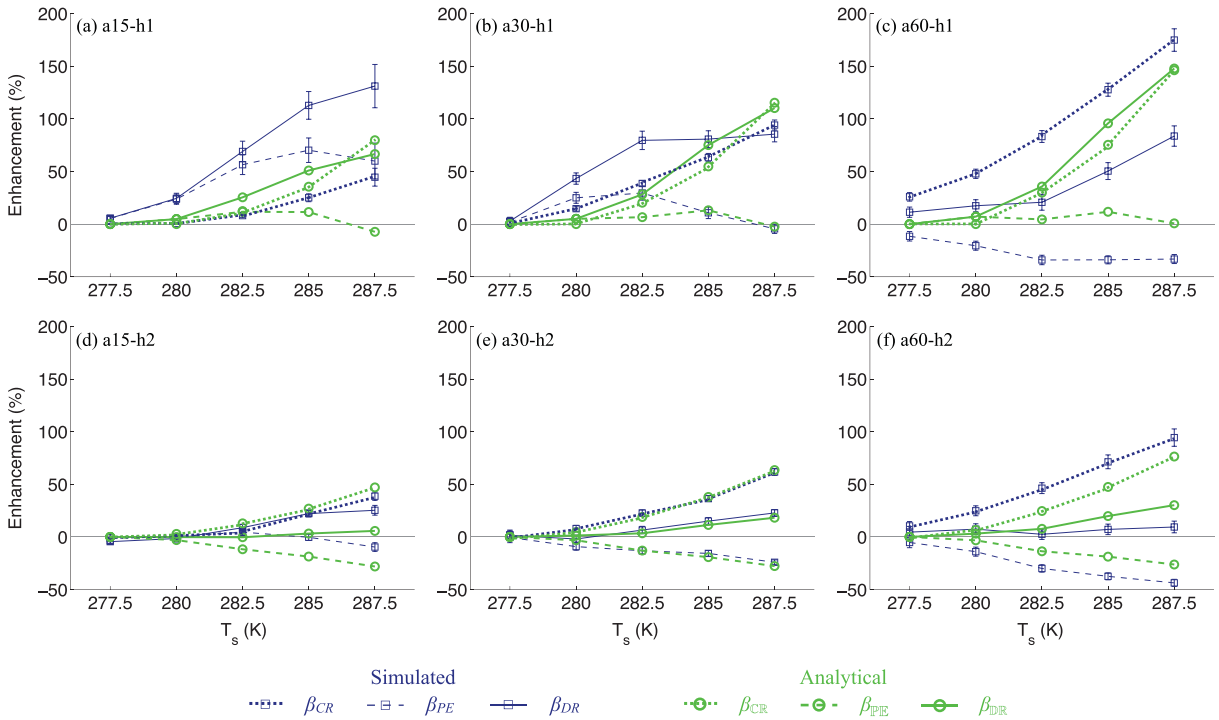

Figure 10. Simulated (black, blue online) and analytically derived (grey, green online) β for each of the non-dimensional diagnostics (Eq. (34)). The cases (a) a15-h1, (b) a30-h1, (c) a60-h1, (d) a15-h2, (e) a30-h2 and (f) a60-h2 are shown. In each panel, β_{CR} and $\beta_{\mathbb{CR}}$ are dotted, β_{PE} and $\beta_{\mathbb{PE}}$ are dashed and β_{DR} and $\beta_{\mathbb{DR}}$ are solid. Error bars are as in Figure 5. This figure is available in colour online at wileyonlinelibrary.com/journal/qj

© 2013 The Authors. *Quarterly Journal of the Royal Meteorological Society* published by John Wiley & Sons Ltd on behalf of the Royal Meteorological Society.

knowledge, this is the first analytical model that captures the effects of both mixed-phase microphysics and embedded convection simultaneously. The model applies strictly to unblocked and unsaturated upstream flows that are not seeded by large-scale precipitation.

Mixed-phase stratiform cloud processes are modelled using a novel two-layer, nonlinear formulation in which snow formation occurs in the upper ('frozen') layer and rain formation occurs in the lower ('liquid') layer (snow is assumed to melt instantaneously in the liquid layer). Whilst a two-layer approach has been used previously in the linear model of Barstad and Schüller (2011), the nonlinear formulation used here does not arbitrarily constrain the precipitation formation time-scales, but rather predicts them using simplified bulk equations for vapour deposition and accretion in the frozen layer and autoconversion, collision and coalescence in the liquid layer.

In addition, a unique feature of this model is its consideration of convective processes which, due to their formidable complexity, have until now been neglected in comparable models. Convection is represented through a simple adiabatic sorting model for buoyant ascent and compensating descent plus a simple detrainment formulation.

Overall, the simulations and analytical model agree that taller and wider mountains generally yield the largest drying ratio (at least for unblocked flows). Although the drying ratio generally decreases over shorter and/or narrower mountains, this decrease may be offset by embedded convection, which can greatly enhance precipitation in otherwise inefficient clouds. The inclusion of embedded convection in the analytical model allowed it to capture several key trends that explain this precipitation enhancement. The most robust of these is the combination of enhanced cloud condensation and precipitation formation, along with enhanced cloud evaporation, as the moist instability increases. The degree of cancellation between these trends, which is smallest over short and narrow mountains, controls the ability of embedded convection to enhance orographic precipitation.

By taking an idealized atmospheric profile (defined with constant wind speed, relative humidity and Brunt–Väisälä frequency), along with the dimensions (width and height) of an idealized mountain ridge, the model computes adiabatic lifting profiles for air parcels beginning at each vertical level. These are then used to determine a full suite of bulk (volume-integrated) diagnostics that characterize the amount of condensation, evaporation, precipitation formation and precipitation sedimentation (fallout). To calculate the diagnostics of a convection-permitting orographic flow, the contributions for a purely mechanically lifted (non-convective) flow and a fully convective flow are combined using simple weighting functions based on three important time-scales: (i) the advective time-scale (τ_a) governing the amount of time parcels experience orographic lifting; (ii) the time-scale for mechanical lifting to the level of free convection (τ_{LFC}); and (iii) the convective time-scale (τ_{CONV}), which controls the time taken for convective cells to develop.

Throughout most of the parameter space considered, the model successfully reproduced the precipitation amounts and sensitivities in the simulations of Cannon *et al.* (2012). Nevertheless, the results suggest that the influence of convection may be overestimated over short and narrow mountains. In addition, the tendency for precipitation efficiency to reduce with increased mountain width in the convection-permitting simulations was underestimated. These discrepancies may be associated with the neglect of convective entrainment, which could significantly influence the condensation and cloud evaporation rates. They may also relate to oversimplified one-dimensional lifting profiles that do not take mountain width properly into account or to the neglect of the impact of dynamical enhancement of convection over steeper slopes (Kirshbaum and Smith, 2008). The resolution of this issue may help determine why enhanced cloud evaporation does not completely offset the increase in condensation due to embedded convection over short and narrow mountains, as it does over tall and wide mountains.

Further improvements could be made by introducing more vertical layers and by lifting the air incrementally, thus discretizing the model. While increasing its complexity, spatial variability is known to have important implications for microphysical mechanisms that are sensitive to the local thermodynamic conditions within clouds (Bader and Roach, 1977; Kunz and Kottmeier, 2006). The model could also be extended to three dimensions, either by discretization in both x and y or by using linear gravity wave theory to calculate condensation (Smith and Barstad, 2004). In addition, the model could be adapted to include graupel as well as microphysical processes such as ice-phase latent heating and ice splintering. These were neglected here, as they had little influence on precipitation formation in the simulations. Finally, although it does not currently account for changing aerosol loading, the model could incorporate this by making the autoconversion time-scale dependent on the cloud condensation nuclei concentration (Stevens and Seifert, 2008) and permitting the snow size distribution parameter to vary with the ice nuclei concentration.

In addition to generally advancing the theoretical understanding of orographic precipitation, this analytical model may be used to understand better the sensitivities of orographic precipitation to changing environmental conditions. After the above improvements are implemented, the model may provide a means for computationally efficient regional climate downscaling and could also be used to help interpret real orographic precipitation events. An improved theoretical understanding of orographic precipitation may also help to inform future developments in convection parametrizations, which currently suffer from significant systematic biases in mountainous regions (Schwitalla *et al.*, 2008; Wulfmeyer *et al.*, 2008).

Acknowledgements

We thank Dr Maarten Ambaum, Professor Robin Hogan and Professor George Craig for helpful conversations throughout the course of this work. This research project was supported by a PhD studentship (grant number NE/G001685/1) from the Natural Environment Research Council (NERC).

Appendix A: Partial formation rates for stratiform clouds

In this Appendix, derivations are presented for the (nonlinear) formation rate associated with purely mechanically lifted flows. The contributing partial formation rates are described in turn in sections A.1–A.4, after which the behaviour of the solution and its sensitivity to uncertain model parameters is discussed in sections A.5–A.6.

Adapting the method of Jiang and Smith (2003), a steady-state equation representing the conservation of cloud water mass in the frozen layer (M_{cf}) can be written as

$$\frac{\mathrm{d}M_{cf}}{\mathrm{d}t} = \mathbb{C}_f - \mathbb{VDEP} - \mathbb{ACC} - \frac{M_{cf}}{\tau_a} = 0, \qquad \text{(A1)}$$

where M_{cf}/τ_a represents the rate of advection of cloud water to the lee where it evaporates (this term is considered linear, as τ_a is independent of M_{cf}). The equivalent expression for snow mass, M_{sn}, in the frozen layer is

$$\frac{\mathrm{d}M_{sn}}{\mathrm{d}t} = \mathbb{VDEP} + \mathbb{ACC} - M_{sn}\left(\frac{1}{\tau_a} + \frac{1}{\tau_{melt}}\right) = 0, \qquad \text{(A2)}$$

where the two terms in parentheses correspond to the linear advection of snow to the lee and the linear sedimentation of snow from the frozen to the liquid layer. The time-scale for snow to sediment to the liquid layer and (instantaneously) melt to

© 2013 The Authors. *Quarterly Journal of the Royal Meteorological Society* published by John Wiley & Sons Ltd on behalf of the Royal Meteorological Society.

form rain is $\tau_{\rm melt} = (z_{\rm sn} - z_{\rm f})/v_{\rm sn}$, which is the distance between the average snow formation height ($z_{\rm sn}$) and the top of the liquid layer ($z_{\rm f}$), divided by the fall speed of snow, $v_{\rm sn} = 1\,{\rm m\,s^{-1}}$ (for simplicity this is assumed constant). $z_{\rm sn}$ is approximated as the condensate-weighted height of the frozen layer, where the total condensate at each level is determined by the sum of the contributions from the adiabatic ascent of all layers below it. Combining Eqs (A1) and (A2) gives

$$M_{\rm cf} = \mathbb{C}_{\rm f}\tau_{\rm a} - M_{\rm sn}\left(1 + \frac{\tau_{\rm a}}{\tau_{\rm melt}}\right), \tag{A3}$$

and so, for each case, $M_{\rm cf}$ varies only with $M_{\rm sn}$ (which is as yet unknown). As will be shown in the following two subsections, expressions can be derived for both $\mathbb{VDEP}$ and $\mathbb{ACC}$ that, for each case, are also only functions of $M_{\rm sn}$, allowing the equations to be solved iteratively.

Following the same methodology as for the frozen layer, the cloud water mass ($M_{\rm cl}$) and rain mass ($M_{\rm r}$) conservation equations for the liquid layer can be written respectively as

$$\frac{{\rm d}M_{\rm cl}}{{\rm d}t} = \mathbb{C}_{\rm l} - \mathbb{AUT} - \mathbb{COCO} - \frac{M_{\rm cl}}{\tau_{\rm a}} = 0, \tag{A4}$$

$$\frac{{\rm d}M_{\rm r}}{{\rm d}t} = \mathbb{AUT} + \mathbb{COCO} + \frac{M_{\rm sn}}{\tau_{\rm melt}} - M_{\rm r}\left(\frac{1}{\tau_{\rm a}} + \frac{1}{\tau_{\rm r,sed}}\right) = 0, \tag{A5}$$

where $M_{\rm sn}/\tau_{\rm melt}$ is the rate at which snow melts into the layer from above. Rain is lost from the liquid layer through both linear advection to the lee and linear sedimentation to the ground. The time-scale for the latter is given by $\tau_{\rm r,sed} = z_{\rm r}/v_{\rm r}$, which is the height of rain formation ($z_{\rm r}$) divided by a (constant) fall velocity of rain, $v_{\rm r} = 5\,{\rm m\,s^{-1}}$. As in the calculation of $\tau_{\rm melt}$, the formation height is approximated as a condensate-weighted height in the layer. These equations can be combined to yield

$$M_{\rm cl} = \tau_{\rm a}\mathbb{C}_{\rm l} + M_{\rm sn}\frac{\tau_{\rm a}}{\tau_{\rm melt}} - M_{\rm r}\left(1 + \frac{\tau_{\rm a}}{\tau_{\rm r,sed}}\right) \tag{A6}$$

and so for each case $M_{\rm cl}$ is a function of $M_{\rm sn}$, which is determined from the frozen layer, and $M_{\rm r}$. As will be shown in the following two subsections, expressions can be derived for both $\mathbb{AUT}$ and $\mathbb{COCO}$ that, for each case, are also only functions of $M_{\rm r}$ and the liquid layer equations can also be solved iteratively (once the frozen layer equations have been solved).

A.1. Deposition to snow

When saturated air above the freezing level is lifted, a proportion of the water vapour deposits directly to snow at the expense of supercooled cloud water (the so-called 'Bergeron' mechanism). Here, we model this process by assuming that the compensatory evaporation of cloud water to vapour occurs instantaneously and so $\mathbb{VDEP}$ is effectively a pathway from cloud water to snow.

The deposition rate is modelled on the fundamental principle of diffusional growth along a density gradient. This occurs when the vapour density just above the surface of an ice crystal, which is assumed equal to the saturation vapour pressure with respect to ice ($\rho_{\rm vi}$), is less than that of the surrounding atmosphere. By analogy with electrostatics, the deposition rate of vapour on to a snow hydrometeor can be written as $4\pi\delta_{\rm v}(D/2)(\rho_{\rm v} - \rho_{\rm vi})$ (eq. (9.2) of Rogers and Yau, 1989), where $\delta_{\rm v} = 0.211\,{\rm cm^2\,s^{-1}}$ is the diffusivity of water vapour in air and $D/2$ is the capacitance of spherical snow hydrometeors with varying diameter D. This simplification (snow is not spherical but usually consists of fractal-like aggregates) is accounted for in the Thompson microphysics scheme employed in the simulations through the use of a non-spherical mass–diameter relationship (Thompson *et al.*, 2008). Although, for simplicity, snow is assumed spherical for the deposition (and accretion) rates, the mass–diameter relationship used is the same as that employed by the Thompson microphysics scheme.

As vapour deposits on to snow, latent heat is released, which effectively increases $\rho_{\rm vi}$ and reduces the deposition rate (Rogers and Yau, 1989). Testing with different formulations suggested that the inclusion of this effect is critical to produce a solution that supports snow generation (not shown). From eq. (9.4) of Rogers and Yau (1989), which includes the effect of this latent heating and associated heat transfer away from the surface, a deposition rate can be defined as

$$\mathbb{VDEP} = a_{\rm c}\left(\frac{l_z}{2} - z_{\rm f}\right) \times \int_0^\infty \frac{2\pi D}{\mathfrak{C}_{\rm VDEP}}\overline{\left(\frac{e}{e_{\rm i}} - 1\right)}N_{\rm sn}(D)\,{\rm d}D, \tag{A7}$$

where

$$\mathfrak{C}_{\rm VDEP} = \left(\frac{L_{\rm SUB}}{R_{\rm v}\overline{T}} - 1\right)\frac{L_{\rm SUB}}{\kappa\overline{T}} + \frac{R_{\rm v}\overline{T}}{\overline{e_{\rm i}}\delta_{\rm v}}. \tag{A8}$$

In Eq. (A7), e is the vapour pressure and $e_{\rm i}$ is the saturated vapour pressure with respect to ice, whilst $N_{\rm sn}(D)$ represents the number density of snow hydrometeors of size D. In (A8), $L_{\rm SUB} = 2.834 \times 10^6\,{\rm J\,kg^{-1}}$ is the latent heat of sublimation, $\kappa = 2.43 \times 10^{-2}\,{\rm J\,m^{-1}\,s^{-1}\,K^{-1}}$ is the thermal conductivity of air and $R_{\rm v} = 461.6\,{\rm J\,kg^{-1}\,K}$ is the gas constant of water vapour. In these equations, overlines represent an influx-weighted average over the frozen layer after each level has been raised adiabatically to $z_{\rm lift,\,LAM}$. The local deposition rate is integrated over the hydrometeor size distribution for all possible values of D (0 to ∞) and also over the layer via the factor $a_{\rm c}\left(\frac{1}{2}l_z - z_{\rm f}\right)$. Note that, while very large diameters are not excluded in this distribution, $N_{\rm sn}(D) \to 0$ as $D \to \infty$.

For simplicity, $N_{\rm sn}(D)$ follows a Marshall–Palmer distribution as described by Gunn and Marshall (1958),

$$N_{\rm sn}(D) = N_{0,{\rm sn}}{\rm e}^{-\lambda_{\rm sn}D}, \tag{A9}$$

where $N_{0,{\rm sn}}$ is the distribution intercept parameter and $\lambda_{\rm sn}$ is the distribution slope parameter. As noted by Houze *et al.* (1979), typical values for $N_{0,{\rm sn}}$ can vary considerably with temperature. Here we follow Lin *et al.* (1983), who used $N_{0,{\rm sn}} = 3 \times 10^6\,{\rm m^{-4}}$. $\lambda_{\rm sn}$ is determined by integrating $m_{\rm sn}(D)N_{\rm sn}(D)$ from $D = 0 \to \infty$ and over the layer, where $m_{\rm sn}(D)$ (kg) is the mass of a snow hydrometeor of characteristic size D, and equating this to $M_{\rm sn}$. In the simulations, $m_{\rm sn}(D) = 0.069D^2$ (Thompson *et al.*, 2008) and so, utilizing this relation along with the mathematical relation $\int_0^\infty D^b{\rm e}^{-\lambda_{\rm sn}D}\,{\rm d}D = \Gamma(1+b)/\lambda^{1+b}$ (where Γ indicates a Gamma function and, in this case, $b = 2$), the general formulation for the snow distribution slope parameter is derived as

$$\lambda_{\rm sn} = \left[\frac{0.069\,N_{0,{\rm sn}}\,a_{\rm c}\,\left(\frac{1}{2}l_z - z_{\rm f}\right)\,\Gamma(3)}{M_{\rm sn}}\right]^{1/3}. \tag{A10}$$

Note that, because $M_{\rm sn}$ controls the shape of the mass-size distribution, a larger $M_{\rm sn}$ implies both a larger total number of hydrometeors and a greater proportion of larger hydrometeors. By using this definition of $\lambda_{\rm sn}$ together with Eq (A9), Eq (A7) can be solved to find

$$\mathbb{VDEP} = \frac{2\pi a_{\rm c}\,(l_z/2 - z_{\rm f})\,\overline{[(e/e_{\rm i}) - 1]}N_{0,{\rm sn}}}{\mathfrak{C}_{\rm VDEP}\lambda_{\rm sn}^2}, \tag{A11}$$

which for each case varies only with $M_{\rm sn}$.

© 2013 The Authors. *Quarterly Journal of the Royal Meteorological Society* published by John Wiley & Sons Ltd on behalf of the Royal Meteorological Society.

A.2. The accretion of cloud water by snow

As in the nonlinear analytical model of Jiang and Smith (2003), the rate at which snow accretes cloud water is determined by assuming that spherical snow hydrometeors 'collect' cloud water (which is homogeneously spread throughout the layer with density $\rho_{\rm cf}$) at a rate

$$\mathbb{ACC} = a_{\rm c}\left(\frac{l_z}{2} - z_{\rm f}\right) \times \int_0^\infty \frac{\pi D^2}{4}\rho_{\rm cf}E_{\rm sn}\nu_{\rm sn}N_{\rm sn}(D)\,{\rm d}D, \tag{A12}$$

where $E_{\rm sn}$ is the accretion efficiency for snow. This efficiency is difficult to estimate, but can be considerably less than unity due to the tendency for cloud droplets to be deflected along flow streamlines around the hydrometeor (Pruppacher and Klett, 1978). In reality, this efficiency also depends on the relative size and velocity of the hydrometeors, turbulence, electrostatic effects and whether or not aggregation or fragmentation occurs upon collision (Pruppacher and Klett, 1978). Such effects are, however, beyond the scope of this analytical model and for simplicity $E_{\rm sn} = 0.4$ is treated as a constant (which has been tuned for best agreement with the simulations).

Combining Eqs (A9) and (A10) with Eq. (A12) yields

$$\mathbb{ACC} = \frac{\pi E_{\rm sn}\nu_{\rm sn}N_{0,\rm sn}M_{\rm cf}}{2\lambda_{\rm sn}^3}, \tag{A13}$$

which for each case varies only with $M_{\rm cf}$ and $M_{\rm sn}$. As $M_{\rm cf}$ also only varies with $M_{\rm sn}$ through Eq. (A3), $M_{\rm sn}$ is once again the only remaining unknown.

A.3. The autoconversion of cloud water to rain

Cloud droplets grow via condensation of water vapour and by collision and coalescence with other cloud droplets and, once large enough, form rain drops. Though important for initiating raindrop production, this process of 'autoconversion' accounts for only a small proportion of the total formation rate in the simulations. A less accurate (i.e. linear) treatment is thus deemed sufficient for our purposes. The autoconversion rate,

$$\mathbb{AUT} = \frac{\max\left(M_{\rm cl} - M_{\rm cl}^*,\,0\right)}{\tau_{\rm aut}}, \tag{A14}$$

is defined as a linear function of cloud mass, but with a threshold to ensure that no rain can form via autoconversion in sparse clouds (as proposed by Kessler, 1969). The threshold mass, $M_{\rm cl}^* = a_{\rm c}z_{\rm f}\rho_{\rm cl}^*$, corresponds to a cloud density of $\rho_{\rm cl}^* = 1\,{\rm g\,m^{-3}}$ (within the typical range; see for example Lin *et al.*, 1983; Thompson *et al.*, 2004) and $\tau_{\rm aut} = 1000\,{\rm s}$ is a typical autoconversion time-scale (as in Rutledge and Hobbs, 1983; Thompson *et al.*, 2004; Stevens and Seifert, 2008). As a result, for each case the only remaining unknown parameters upon which $\mathbb{AUT}$ depends are $M_{\rm sn}$ and $M_{\rm r}$ (through Eqs (A6) and (A14)).

A.4. The collision and coalescence of cloud water by rain

The process of collection and coalescence of cloud water by falling rain drops can be described in a form analogous to the accretion of cloud water by falling snow in section A.2. Following the derivation of Eq. (A13), with the appropriate substitutions for liquid layer cloud and rain substance, leads to

$$\mathbb{COCO} = \frac{\pi E_{\rm r}\nu_{\rm r}N_{0,\rm r}M_{\rm cl}}{2\lambda_{\rm r}^3}, \tag{A15}$$

where the rain distribution intercept parameter is $N_{0,\rm r} = 8\times10^6\,{\rm m^{-4}}$ (Lin *et al.*, 1983). The distribution slope parameter is given by $\lambda_{\rm r}$ (defined later), whilst $E_{\rm r} = 0.6$ represents a (constant) efficiency with which rain drops collide and coalesce with cloud water within the sweep volume (which, as for $E_{\rm sn}$, is tuned for best agreement with the simulations). Implicit in Eq. (A15) is the assumption of a Marshall–Palmer distribution for the number of rain drops,

$$N_{\rm r}(D) = N_{0,\rm r}{\rm e}^{-\lambda_{\rm r}D}, \tag{A16}$$

of diameter D. This distribution is identical to that described by Eq. (A9) except for proper substitution for rain water substance. Following the same method as in the derivation of Eq. (A10), the distribution slope $\lambda_{\rm r}$ can be determined by integrating $m_{\rm r}(D)N_{\rm r}(D)$ over all D and over the liquid layer and equating it to the total mass of rain $M_{\rm r}$. Rain drops are assumed spherical and so $m_{\rm r} = (\pi/6)\widehat{\rho}_{\rm r}D^3$ is the mass of a single raindrop and $\widehat{\rho}_{\rm r} = 1000\,{\rm kg\,m^{-3}}$ is the density of water. The rain distribution slope parameter is thus calculated as

$$\lambda_{\rm r} = \left[\frac{\pi\widehat{\rho}_{\rm r}N_{0,\rm r}a_{\rm c}z_{\rm f}\Gamma(4)}{6M_{\rm r}}\right]^{1/4}. \tag{A17}$$

By combining Eqs (A6), (A15) and (A17), one can see that for each case $\mathbb{COCO}$ also varies with $M_{\rm sn}$ and $M_{\rm r}$ only.

A.5. Behaviour of the nonlinear solution

The frozen layer equations (Eqs (A2), (A3), (A11) and (A13)) can be solved iteratively by expressing $M_{\rm cf}$, $\mathbb{VDEP}$ and $\mathbb{ACC}$ (and thus the 'actual' snow mass, $M_{\rm sn}$) as a function of an 'estimate' snow mass, $M'_{\rm sn}$. Solutions to this set of equations are found at points that satisfy $M_{\rm sn} = M'_{\rm sn}$. The liquid layer equations are analogously solved, with $M_{\rm cl}$, $\mathbb{AUT}$ and $\mathbb{COCO}$ (and thus the 'actual' rain mass, $M_{\rm r}$) written as a function of an estimate rain mass $M'_{\rm r}$ by combining Eqs (A5), (A6), (A14) and (A15) and using the value of $M_{\rm sn}$ as previously calculated from the frozen layer. Solutions are found at points that satisfy $M_{\rm r} = M'_{\rm r}$.

Figure A1 shows the dependence of these variables on $M'_{\rm sn}$ and $M'_{\rm r}$ for the a30-h1-LAM-T277 and a30-h1-LAM-T287 cases. For clarity, each variable has been normalized by the area of the relevant layer, so that the masses become densities (ρ) and the total formation rates become local formation rates (depicted in a lower case and standard font). As the estimated snow density ($\rho'_{\rm sn}$) increases, $\rho_{\rm cf}$ decreases accordingly due to the enforced conservation of water within the layer. The deposition rate increases monotonically with $\rho'_{\rm sn}$, as it depends only on the supersaturation with respect to ice and the amount of snow (Figure A1, panel (a)). In contrast, the rate of autoconversion of cloud water to rain decreases monotonically with $\rho'_{\rm r}$, as it does not explicitly depend on the presence of rain drops (Figure A1, panel (b)). Both the accretion, collision and coalescence rates increase to a maximum, after which they decrease as the benefit of increased snow or rain becomes outweighed by a lack of cloud water for the precipitation to scavenge. In both layers there are always two solutions, one of which corresponds to a non-precipitating state for which there is no snow or rain. If the other solution, $\rho'_{\rm sn} = \rho_{\rm sn} > 0$ and/or $\rho'_{\rm r} = \rho_{\rm r} > 0$ (depicted by the vertical grey lines in Figure A1), corresponds to a point where $M_{\rm cf}$ or $M_{\rm cl}$ is positive, then the cloud can support precipitation in a steady state. As also found by Jiang and Smith (2003), this bimodal solution arises due to the nonlinear nature of the equations.

A.6. Sensitivity testing

The nonlinear $\mathbb{FE}_{\rm LAM}$ formulation (Eq. (19)) is sensitive to a number of the constants introduced in Appendix A. Over the tallest and widest mountains (where $\mathbb{FE}_{\rm LAM}$ is highest), the

© 2013 The Authors. *Quarterly Journal of the Royal Meteorological Society* published by John Wiley & Sons Ltd on behalf of the Royal Meteorological Society.

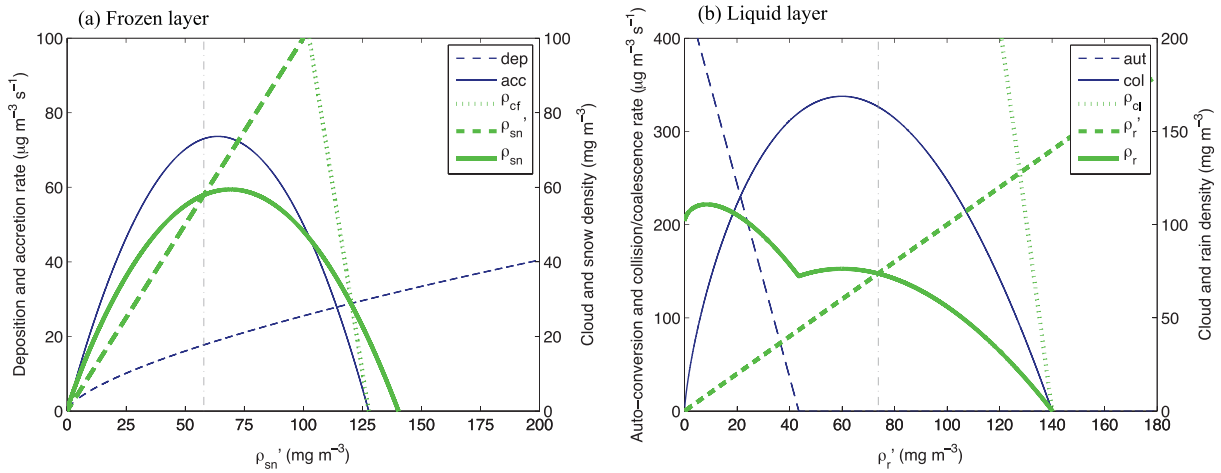

Figure A1. The dependence of cloud and precipitation density (grey, green online), as well as various precipitation formation rates (black, blue online), on the estimated precipitation density. The panels show (a) the frozen layer for the a30-h1-T277 case and (b) the liquid layer for the a30-h1-T287 case. The grey, vertical, dot−dashed lines mark the non-zero solution points. This figure is available in colour online at wileyonlinelibrary.com/journal/qj

results were found to be largely insensitive to these constants. Over the shortest and narrowest mountain, however, significant sensitivities were found. In the a15-h1-LAM-T277 case, $\mathbb{FE}_{\mathrm{LAM}}$ was most sensitive to changes in the accretion efficiency (E_{sn}), where $\mathbb{FE}_{\mathrm{LAM}}$ increased from 0.30 to 0.69 as E_{sn} was increased from 0.4 to 1. Upon halving the efficiency to 0.2, snow production was all but terminated and $\mathbb{FE}_{\mathrm{LAM}}$ decreased to 0.02. Lesser, but still significant, sensitivities were found for the fall velocity of snow (ν_{sn}) and for order-of-magnitude variations in the snow distribution intercept parameter ($N_{0,\,\mathrm{sn}}$). Similarly, in the a15-h1-LAM-T287 case, the largest sensitivity was found with respect to the collision and coalescence efficiency (E_{r}), whereby $\mathbb{FE}_{\mathrm{LAM}}$ increased from 0.35 to 0.52 as E_{r} was increased from 0.6 to 1. Upon halving E_{r} to 0.3, $\mathbb{FE}_{\mathrm{LAM}}$ was reduced to 0.21. Lesser sensitivities were found by varying the rain distribution intercept parameter ($N_{0,\,\mathrm{r}}$) and the autoconversion threshold density (ρ_{cl}^{*}). Whilst the majority of constants throughout this article were chosen to match either the Thompson scheme or values commonly found in the literature, E_{sn} and E_{r} were treated as tunable parameters (within the physically plausible range of 0−1). The values chosen (0.4 and 0.6, respectively) were those that produced the best overall comparison with the simulations. No case-specific tuning was applied.

To illustrate the importance of an accurate prediction of $z_{\mathrm{lift,\,LAM}}$ on $\mathbb{FE}_{\mathrm{LAM}}$, an additional sensitivity test was conducted by replacing $z_{\mathrm{lift,\,LAM}}$ with a uniform lifting assumption ($z + h_{\mathrm{m}}$). This significantly increases $\mathbb{CR}_{\mathrm{LAM}}$, which in turn increases $\mathbb{FE}_{\mathrm{LAM}}$ from 0.30 to 0.63 in the a15-h1-LAM-T277 case and from 0.35 to 0.60 in the a15-h1-LAM-T287 case. This highlights the importance of an accurate lifting profile (and condensation rate) as a prerequisite for an accurate nonlinear formation rate.

Appendix B: Commonly used abbreviations and symbols

To aid the reader, a list of commonly used abbreviations and symbols is provided in Table B1.

Table B1. A list of commonly used abbreviations and symbols. Throughout the article, diagnostics are written in 'blackboard bold' font (e.g. $\mathbb{A}$, $\mathbb{B}$, $\mathbb{C}$) when referring to the analytical model and standard font when referring to the simulations.

Abbreviations and subscripts

LAM	Laminar (without convection)
CONV	Convective
CP	Convection-permitting
LCL	Lifting condensation level
LFC	Level of free convection
LNB	Level of neutral buoyancy
CAPE	Convective available potential energy
ww	Windward slope
lee	Lee slope
sn	Snow
r	Rain
c, cloud	Cloud
p	Precipitation
l	Liquid
f	Frozen, freezing

Dimensional diagnostics (kg m s^{-1})

I	Water vapour influx
C	Condensation rate
E	Evaporation rate
F	Formation rate
$VDEP$	Snow vapour deposition rate
ACC	Snow accretion rate
AUT	Rain autoconversion rate
$COCO$	Rain collision and coalescence rate
$MELT$	Snow melting rate
SUB	Subsidence rate
DET	Detrainment rate
P	Precipitation rate
A	Rate of advection to the lee
O	Water vapour outflux

Miscellaneous symbols (standard SI units)

a_{m}	Mountain width parameter
a_{c}	Cloud width parameter
h_{m}	Peak mountain height
T_{s}	Surface temperature
U	Background cross-ridge wind speed
l_z	Vertical wavelength of a dry, linear, hydrostatic and steady mountain wave

Non-dimensional diagnostics

CR	Condensation ratio
EE	Evaporation efficiency
FE	Formation efficiency
FE_{eff}	Effective formation efficiency
FE_{linear}	Linear formation efficiency
DEP	Deposition efficiency
AC	Autoconversion efficiency

© 2013 The Authors. *Quarterly Journal of the Royal Meteorological Society* published by John Wiley & Sons Ltd on behalf of the Royal Meteorological Society.

Table B1. Continued

w_{LAM}	Typical vertical velocity within a stratiform cloud	*COL*	Collection efficiency
		SE	Sedimentation efficiency
w_{CONV}	Typical vertical velocity within a convective updraught	*PE*	Precipitation efficiency
		DR	Drying ratio
γ	Non-dimensional convective scaling constant	β	Enhancement parameter
α	Non-dimensional weighting function for stratiform or convective cloud processes		

Parcel trajectory levels (m)

z_i	Initial height
z_{LCL}	Height of the LCL
z_{LFC}	Height of the LFC
z_{LNB}	Height of the LNB
z_f	Height of the atmospheric freezing level
z_l	Height of an ascending air parcel
z_{lift}	Maximum height of an ascending air parcel
z_{fin}	Height of an air parcel after undergoing convective subsidence

Time-scales (s)

τ_a	Advection through the orographic cloud
τ_{LFC}	Mechanical lifting to the LFC
τ_{CONV}	Convective overturning
τ_{LAM1}	Advection to the lee *without* passing the LFC
τ_{LAM2}	Advection to the lee *after* passing the LFC
τ_{form}	Precipitation formation
$\tau_{r,\,sed}$	Rain sedimentation (fallout)
τ_{melt}	Snow sedimentation to z_f and subsequent melting to form rain
$\tau_{sn,\,sed}$	Snow sedimentation to z_f, melting and sedimentation to the surface as rain
τ_e	Lee side precipitation evaporation

References

Bader MJ, Roach WT. 1977. Orographic rainfall in warm sectors of depressions. *Q. J. R. Meteorol. Soc.* **103**: 269–280.

Barstad I, Schüller F. 2011. An extension of Smith's linear theory of orographic precipitation: Introduction of vertical layers. *J. Atmos. Sci.* **68**: 2695–2709.

Barstad I, Grabowski WW, Smolarkiewicz PK. 2007. Characteristics of large-scale orographic precipitation: Evolution of linear model in idealised problems. *J. Hydrol.* **340**: 78–90.

Bougeault P, Binder P, Buzzi A, Dirks R, Houze R, Kuettner J, Smith RB, Steinacker R, Volkert H. 2001. The MAP special observing period. *Bull. Am. Meteorol. Soc.* **82**: 433–462.

Cannon DJ, Kirshbaum DJ, Gray SL. 2012. Under what conditions does embedded convection enhance orographic precipitation? *Q. J. R. Meteorol. Soc.* **138**: 391–406.

Choularton TW, Perry SJ. 1986. A model of the orographic enhancement of snowfall by the seeder-feeder mechanism. *Q. J. R. Meteorol. Soc.* **112**: 335–345.

Damiani R, Zehnder J, Geerts B, Demko J, Haimov S, Petti J, Poulos GS, Razdan A, Hu J, Leuthold M, French J. 2008. The cumulus, photogrammetric, in situ, and Doppler observations experiment of 2006. *Bull. Am. Meteorol. Soc.* **89**: 57–73.

Fuhrer O, Schär C. 2005. Embedded cellular convection in moist flow past topography. *J. Atmos. Sci.* **62**: 2810–2828.

Gunn KLS, Marshall JS. 1958. The distribution with size of aggregate snowflakes. *J. Meteorol.* **15**: 452–461.

Hobbs PV, Easter RC, Fraser AB. 1973. A theoretical study of the flow of air and fallout of solid precipitation over mountainous terrain. Part II: Microphysics. *J. Atmos. Sci.* **30**: 813–823.

Hong S-Y, Dudhia J, Chen S-H. 2004. A revised approach to ice microphysical processes for the bulk paramterization of clouds and precipitation. *Mon. Weather Rev.* **132**: 103–120.

Houze RA, Hobbs PV, Herzegh PH, Parsons DB. 1979. Size distributions of precipitation particles in frontal clouds. *J. Atmos. Sci.* **36**: 156–162.

Jiang Q, Smith RB. 2003. Cloud timescale and orographic precipitation. *J. Atmos. Sci.* **60**: 1543–1559.

Kain JS. 2004. The Kain–Fritsch convective parameterisation: An update. *J. Appl. Meteorol.* **43**: 170–181.

Kain JS, Fritsch JM. 1990. A one-dimensional entraining plume model and its application in convective parameterization. *J. Atmos. Sci.* **47**: 2784–2802.

Kain JS, Fritsch JM. 1993. *Convective Parameterization for Mesoscale Models: The Kain–Fritsch Scheme*, The Representation of Cumulus Convection in Numerical Models, Meteorological Monographs **24**. American Meteorological Society: Boston, MA; 165–170.

Kessler E. 1969. *On the Distribution and Continuity of Water Substance in Atmospheric Circulation*, Meteorological Monographs **32**. American Meteorological Society: Boston, MA.

Kirshbaum DJ, Durran DR. 2004. Factors governing cellular convection in orographic precipitation. *J. Atmos. Sci.* **61**: 682–698.

Kirshbaum DJ, Smith RB. 2008. Temperature and moist-stability effects on mid-latitude orographic precipitation. *Q. J. R. Meteorol. Soc.* **134**: 1183–1199.

Kirshbaum DJ, Smith RB. 2009. Orographic precipitation in the tropics: Large-eddy simulations and theory. *J. Atmos. Sci.* **66**: 2559–2578.

Kunz M, Kottmeier C. 2006. Orographic enhancement of precipitation over low mountain ranges. Part I: Model formulation and idealized simulations. *J. Appl. Meteorol. Climatol.* **45**: 1025–1040.

Lin Y-L, Farley RD, Orville HD. 1983. Bulk parameterization of the snow field in a cloud model. *J. Clim. Appl. Meteorol.* **22**: 1065–1092.

Morrison H, Pinto JO. 2005. Mesoscale modeling of springtime Arctic mixed-phase stratiform clouds using a new two-moment bulk microphysics scheme. *J. Atmos. Sci.* **62**: 3683–3704.

Morrison H, Thompson G. 2009. Impact of cloud microphysics on the development of trailing stratiform precipitation in a simplified squall line: Comparison of one- and two-moment schemes. *Mon. Weather Rev.* **137**: 991–1007.

Morrison H, Curry JA, Khvorostyanov VI. 2005. A new double-moment microphysics parameterization for application in cloud and climate models. Part I: Description. *J. Atmos. Sci.* **62**: 1665–1677.

Pruppacher HR, Klett JD. 1978. *Microphysics of Clouds and Precipitation*. D. Reidel: Dordrecht.

Renno NO, Ingersoll AP. 1996. Natural convection as a heat engine: A theory for CAPE. *J. Atmos. Sci.* **53**: 572–585.

Rogers RR, Yau MK. 1989. *A Short Course in Cloud Physics*. Butterworth-Heineman: Woburn, MA.

Rotunno R, Ferretti R. 2001. Mechanisms of intense Alpine rainfall. *J. Atmos. Sci.* **58**: 1732–1749.

Rutledge SA, Hobbs PV. 1983. The mesoscale and microscale structure and organisation of clouds and precipitation in midlatitude cyclones. VIII: A model for the 'seeder-feeder' process in warm-frontal rainbands. *J. Atmos. Sci.* **40**: 1185–1206.

Sarker RP. 1967. Some modifications in a dynamical model of orographic rainfall. *Mon. Weather Rev.* **95**: 673–684.

Sawyer JS. 1956. The physical and dynamical problems of orographic rain. *Weather* **11**: 375–381.

Schwitalla T, Bauer H-S, Wulfmeyer V, Zängl G. 2008. Systematic errors of QPF in low-mountain regions as revealed by MM5 simulations. *Meteorol. Z.* **17**: 903–919.

Skamarock WC, Klemp JB, Dudhia J, Gill DO, Barker DM, Duda MG, Huang X-Y, Wang W, Powers JG. 2008. '*A description of the Advanced Research WRF version 3*', Technical Report TN-475. NCAR: Boulder, CO.

Smith RB. 1979. The influence of mountains on the atmosphere. *Adv. Geophys.* **21**: 87–230.

Smith RB, Barstad I. 2004. A linear theory of orographic precipitation. *J. Atmos. Sci.* **61**: 1377–1391.

Smith RB, Jiang Q, Fearon MG, Tabary P, Dorninger M, Doyle JD, Benoit R. 2003. Orographic precipitation and air mass transformation: An Alpine example. *Q. J. R. Meteorol. Soc.* **129**: 433–454.

Smith RB, Barstad I, Bonneau L. 2005. Orographic precipitation and Oregon's climate transition. *J. Atmos. Sci.* **62**: 177–191.

© 2013 The Authors. *Quarterly Journal of the Royal Meteorological Society* published by John Wiley & Sons Ltd on behalf of the Royal Meteorological Society.

Stevens B, Seifert A. 2008. Understanding macrophysical outcomes of microphysical choices in simulations of shallow cumulus convection. *J. Meteorol. Soc. Jpn.* **86A**: 143–162.

Stoelinga MT, Hobbs PV, Mass CF, Locatelli JD, Colle BA, Houze Jr RA, Rangno AL, Bond NA, Smull BF, Rasmussen RM, Thompson G, Colman BR. 2003. Improvement of microphysical parameterization through observational verification experiment. *Bull. Am. Meteorol. Soc.* **84**: 1807–1826.

Thompson G, Rasmussen RM, Manning K. 2004. Explicit forecasts of winter precipitation using an improved bulk microphysics scheme. Part I: Description and sensitivity analysis. *Mon. Weather Rev.* **132**: 519–542.

Thompson G, Field PR, Rasmussen RM, Hall WD. 2008. Explicit forecasts of winter precipitation using an improved bulk microphysics scheme. Part II: Implementation of a new snow parameterization. *Mon. Weather Rev.* **136**: 5095–5115.

Wulfmeyer V, Behrendt A, Bauer H-S, Kottmeier C, Corsmeier U, Blyth A, Craig G, Schumann U, Hagen M, Crewell S, Girolamo PD, Flamant C, Miller M, Montani A, Mobbs S, Richard E, Rotach MW, Arpagaus M, Russchenberg H, Schlüssel P, König M, Gärtner V, Steinacker R, Dorninger M, Turner DD, Weckwerth T, Hense A, Simmer C. 2008. The convective and orographically induced precipitation study: A research and development project of the World Weather Research Program for improving quantitative precipitation forecasting in low-mountain regions. *Bull. Am. Meteorol. Soc.* **89**: 1477–1486.

© 2013 The Authors. *Quarterly Journal of the Royal Meteorological Society* published by John Wiley & Sons Ltd on behalf of the Royal Meteorological Society.